1   **REVISION 3**

2

3   **Trioctahedral Fe-rich micas: relationships between magnetic behavior**

4   **and crystal chemistry**

5   Maria Franca Brigatti[1], Marco Affronte[2], Chiara Elmi[1], Daniele Malferrari[1], Angela Laurora[1].

6

7   *[1]Dipartimento di Scienze Chimiche e Geologiche, Università di Modena e Reggio Emilia, Via S.*

8   *Eufemia, 19, I-41121 Modena, Italy; [2]Dipartimento di Scienze Fisiche, Informatiche e*

9   *Matematiche, Università di Modena e Reggio Emilia, Via G. Campi 213/a, I-41100 Modena, Italy.*

10

11   Corresponding Author: Maria Franca Brigatti: Dipartimento di Scienze Chimiche e Geologiche,

12   Università di Modena e Reggio Emilia, Via S. Eufemia 19, I-41121 Modena, Italy. e-mail:

13   mariafranca.brigatti@unimore.it. Phone: +39 059 2055805;Fax: +39 059 2055887

14

15   Running title: Structure and magnetic properties of trioctahedral micas.

16

17   **Abstract.** Six Fe-bearing mica samples with different Fe ordering, $Fe^{2+}/(Fe^{2+}+Fe^{3+})$ ratio,

18   octahedral and tetrahedral composition were studied. Four micas belong to the phlogopite-annite

19   join (space group $C2/m$), two are Mg-rich annite and two are Fe-rich phlogopite, one is a tetra-

20   ferriphlogopite (space group $C2/m$) and one is Li-rich siderophyllite (space group $C2$). Thus these

21   samples had a different environment around the Fe cations and layer symmetry. These micas were

22   characterized by chemical analyses, single crystal X-ray diffraction, X-ray Absorption

23   Spectroscopy, and magnetic measurements. In samples with Fe mostly in octahedral coordination,

24   dominant magnetic interactions among Fe atoms are ferromagnetic, which reach a maximum at

1

25   higher $Fe^{2+}/(Fe^{2+}+Fe^{3+})$ ratios. Samples with higher $Fe^{2+}/(Fe^{2+}+Fe^{3+})$ ratio are also characterized by

26   higher values of the Curie-Weiss θ constant. Where $Fe^{2+}/(Fe^{2+}+Fe^{3+})$ ratios decrease, θ values also

27   decrease. The Fe^{3+}-rich phlogopite shows predominant Fe^{3+} in tetrahedral coordination and shows

28   anti-ferromagnetic interactions with a negative value of the Curie-Weiss θ constant (i.e. $\theta = - 25$ K).

29   Fe ordering in octahedral *trans*- and in one of the two *cis*-sites accounts for a greater θ value in Li-

30   rich siderophyllite when compared to other samples showing similar octahedral Fe content. Our

31   data suggest that Fe^{3+} cations and other non-ferromagnetic cations hinder long range magnetic

32   ordering. This observation may produce for the different role of octahedral Fe magnetic

33   interactions that can in principle develop along long Fe-rich octahedral chains, when compared to

34   tetrahedral-octahedral interactions that are confined within the layer by the non-ferromagnetic

35   cations of the interlayer. Spin glass behavior is indicated by the dependency of the temperature to

36   produce maxima in the susceptibility curve. These maxima are related to the frequency of the

37   applied AC magnetic field.

38

39   ***Key words:*** Fe-rich micas, X-ray absorption spectroscopy, chemical analysis, single crystal X-ray

40   structure determination, magnetic measurements.

41

42   **Introduction**

43   Magnetic techniques are powerful methods to understand electronic and thermodynamic

44   properties of materials (Catalli et al. 2011; Hsu et al. 2010). When complex materials, such as

45   minerals, are involved, magnetic investigations become extremely challenging. Iron is 40 times

46   more abundant than any other magnetic element in the Earth's crust, which is predominantly

47   composed of silicates, thus suggesting why most magnetic studies on minerals are focused on iron

48   silicates such as pyroxenes (Redhammer et al. 2011; 2012). These minerals represent model

49   systems to study magnetic properties characterized by a competitive interaction within and between

50   the quasi-one-dimensional (1D) infinite chains of transition metal bearing octahedral sites. Micas

51   are typical examples of a layer structure, thus showing properties of quasi-two-dimensional (2D)

52   infinite systems. The characterization of magnetic properties of natural Fe-rich trioctahedral micas

53   was addressed by some authors (Anagnostopoulos et al. 1973; Marcelli et al. 2004; Dunlop et al.

54   2006; Pini et al. 2008, 2012), without however obtaining a full understanding of the role of local

55   topology of Fe atoms on magnetic properties. Even if limited in number, studies devoted to

56   magnetic properties of trioctahedral micas increased significantly in the few past years. These

57   studies, in part were motivated by the abundance of these minerals in nature, but also because of the

58   great variability in content, oxidation condition and local topology of Fe atoms present (Biedermann

59   et al. 2014). The correlation between magnetic properties of natural trioctahedral micas and their

60   crystal chemical and structural features have been explored previously to understand the origin of

61   magnetic properties in minerals and to better characterize their structure, with particular reference

62   for Fe coordination.

63   In trioctahedral micas, the $Fe^{2+}/(Fe^{2+} + Fe^{3+})$ ratio can vary significantly, together with its

64   distribution within the layer. Fe^{3+} was found to occupy both tetrahedral (T) and octahedral (M)

65   positions, whereas Fe^{2+} was located at M positions only (Brigatti and Guggenheim 2002). Fe^{2+} for

66   Mg^{2+} octahedral substitution defines the trioctahedral mica join from phlogopite [$KMg^{2+}_3AlSi_3O_{10}$

                                              3

67   (OH)$_2$] to annite [KFe$^{2+}_3$AlSi$_3$O$_{10}$(OH)$_2$] (Bailey1984). Tetrahedral substitution of Fe^{3+} for Si^{4+}

68   gives tetra-ferriphlogopite [KMg$^{2+}_3$Fe^{3+}Si$_3$O$_{10}$(OH)$_2$] from phlogopite, and tetra-ferri-annite

69   [KFe$^{2+}_3$Fe^{3+}Si$_3$O$_{10}$(OH)$_2$] from annite. In trioctahedral lithian micas the $^{[iv]}$Si$^{4+}_{-1}$ $^{[vi]}$Li$_{-1}$$^{[iv]}$Al $^{[vi]}$Fe^{2+}

70   vector defines the polylithionite [KLi$_2$AlSi$_4$O$_{10}$(F,OH)$_2$]$-$ siderophyllite [KFe$^{2+}_2$AlSi$_4$O$_{10}$(F,OH)$_2$]

71   join (Rieder et al.1998).

72   Octahedrally-coordinated Fe cations are distributed over three crystallographic positions, i.e. in

73   the *trans*-oriented octahedron (M1) and in the two *cis*-oriented octahedra (M2 and M3). M2 and

74   M3 octahedra are symmetrically related in micas belonging to *C*2/*m* space group. Fe is usually

75   disordered in M1, M2, M3 with a slight preference for the M1 site in trioctahedral micas of the

76   phlogopite−annite join, whereas it can be partially ordered in trioctahedral micas of the

77   polylithionite−siderophyllite join where the much larger Li^{1+} and Fe^{2+} cations occupy the *trans*-site

78   and one of the *cis*-oriented octahedral sites (commonly, M3) and Al^{3+} occupies one of the *cis*-sites

79   (commonly, M2) (Brigatti and Guggenheim 2002).

80   An antiferromagnetic behavior was observed for micas at T values close to 10K and in presence

81   of a magnetic field, following from magnetic moments generated by in-plane ferromagnetic

82   interactions involving Fe^{2+}-Fe^{2+} ions (Coey 1985, 1987; Coey and Ghose 1988; Coey et al. 1981,

83   1982, 1984). Possible magnetic ordering was suggested at T values of < 10K and in a strong

84   magnetic field (Ballet and Coey 1982).

85   Beausoleil et al. (1983) demonstrated that magnetic properties for micas, and specifically for

86   trioctahedral micas close to annite in composition, are remarkably anisotropic, with magnetic

87   susceptibility changing in value if measured in-plane or out-of-plane, following their 2D

88   arrangement and crystal chemistry. Fe atoms can interact with neighboring Fe atoms in the

89   octahedral sheet, whereas interactions out of the sheet are commonly with non-magnetic cations.

90   Townsend and Longworth (1985) suggested a positive super-exchange (ferromagnetic)

91   interaction arising from the interaction of neighboring Fe^{3+}- Fe^{3+} ions, thus in contrast to previous

4

92   studies that claimed these cations to be antiferromagnetically coupled (Coey et al. 1981; Ballet and

93   Coey 1982; Ballet et al. 1985).

94   Several studies tried to explain the occurrence of these different experimental results (Coey

95   1985, 1987; Ballet 1986; Townsend 1987; Townsend et al. 1987; Longworth et al. 1987; Marcelli et

96   al. 2004), without however, reaching a final conclusion. Some authors (Christie et al. 1992;

97   Rancourt et al. 1994) observed an antiferromagnetic trend in the susceptibility–temperature curve

98   for annite crystals, and a magnetic ordering at temperature greater than 10K.

99   In this work, six Fe-bearing mica samples, significantly different in Fe composition and Fe

100   coordination, are selected to relate their magnetic behavior to their chemical composition and

101   cation ordering. All the samples studied belong to $1M$ polytype, but differ in their tetrahedral and

102   octahedral composition, $Fe^{2+}/(Fe^{2+}+Fe^{3+})$ ratio, and layer symmetry. Four samples are from the

103   phlogopite–annite join(space group $C2/m$), one is a tetra-ferriphlogopite (space group $C2/m$) and

104   one is a Li-rich siderophyllite (space group $C2$).

105

106   **Samples and Experimental Methods**

107   *Samples*

108   Sample Albano is a ferroan phlogopite from "Peperino Albano" ignimbrite (Albano Laziale,

109   Italy), originating from the top of the eruption cycle of holocrystalline ejecta of Albano Maar lake.

110   The Albano Maar is a multiple tuff ring consisting of five main explosive cycles (Brigatti et al.

111   2005). Holocrystalline ejecta show granular hypidiomorphic to porphyric structures, with

112   clinopyroxene, brownish mica, and leucite as main mineral phases (Laurora et al. 2009).

113   Samples Oquossoc and Bryant Pond are[vi]Al-rich magnesian annites from the peraluminous-

114   granite zone, located in Oquossoc and Bryant Pond areas (northwest part of the State of Maine,

115   USA), respectively. The mineral assemblage ensures that the mica composition is Al, Si and Ti

5

116   saturated. Petrological and mineralogical data of this area and of micas occurring therein can be

117   found in Guidotti et al. (1988).

118   Samples Tapira and Catalão are from Tapira and Catalão alkaline-carbonatite complexes,

119   respectively. These complexes are located into the Alto Paranaíba Igneous Province (APIP) that

120   occupies a northwest-elongated area between the São Francisco Craton and the northeast border of

121   the Paraná Basin (Brazil). Sample Tapira is from a Bebedeurite rock mainly composed of Fe^{3+}-rich

122   phlogopite, variable amounts of clinopyroxene (> 20%), and subordinate perovskite, apatite, calcite,

123   ilmenite, and titaniferous magnetite (Brigatti et al. 1996). Sample Catalão is from a clinopyroxenite

124   rock that contains clinopyroxene, variable amounts of Fe^{3+}-rich phlogopite, and minor amounts of

125   allotriomorphic carbonate and amphibole (Brod et al. 2001).

126   Sample Eurajoki is a lithian siderophyllite from the Väkkärä granite outcropping in the central

127   part of the polyphasic Eurajoki stock, a rapakivi-granite complex in southwestern Finland. Lithian

128   siderophyllite is associated with topaz, microcline, albite and minor monazite, Nb-,Ta-rich

129   cassiterite, bastnaesite, xenotime, columbitethorite (Haapala 1977).

130

131   *Chemical composition and calculation of the chemical formula*

132   Chemical composition (Table 1) was determined on crystals used for single crystal experiments

133   with a wavelength dispersive ARL-SEMQ electron microprobe (operating conditions: 15 kV

134   accelerating voltage; 15 nA sample current; defocused electron beam with a spot of about 4 μm;

135   counting times of 10 s for both peak and background). Analyses and data processing were

136   performed using the Probe software package of Donovan (1995). The following standards were

137   used: microcline (K, Al), albite (Na), spessartine (Mn), ilmenite (Fe, Ti), clinopyroxene (Si, Ca),

138   olivine (Mg), chromite (Cr), fluorite (F), barite (Ba), sphalerite (Zn), and synthetic Rb-rich glass

139   (Rb). The F content was determined via the method reported by Foley (1989). No evidence of

140   volatilization of F was observed. Several spots (up to 6 spots on each fragment) were analyzed to

141 verify sample homogeneity and to obtain a statistically significant average. Rim-core

142 compositional variation was observed to be within 3% of the estimated standard error for each

143 element (3% relative), indicating a high degree of chemical homogeneity. Individual spot analyses

144 for each crystal fragment were averaged. FeO determination followed the procedure by Meyrowitz

145 (1970) with an estimated measured standard deviation of $\sigma < 4\%$.

146   The Li content was determined via laser ablation inductively coupled to plasma mass

147 spectroscopy (LA-ICP-MS, UP 213, New Wave Research), where the ablated material was

148 transported to the quadrupole ICP-MS XSeriesII (Thermo Fischer Scientific). Three line scans

149 traced along the entire crystal and taken at three points over a 60 μm spot at a scan speed of 25 μm/s

150 were performed. The dwell time was set at 20 s. The ablation frequency was 10 Hz in all scans.

151 The ablated aerosol was atomized at 0.68 bar into the plasma of the ICP-MS unit. NIST 612 (a

152 synthetic glass trace-element reference standard) was selected as standard reference used to create

153 the calibration curve. ^{29}Si was selected as the internal standard. The data obtained were then

154 normalized to the sample SiO_2 content, as measured via electron microprobe analysis. The $(OH)^-$

155 content was derived from thermo-gravimetric analysis in He gas flow using a Seiko SSC 5200

156 thermal analyzer (heating rate 10 °C/min and gas flow rate 100 μl/min) equipped with a mass

157 spectrometer (GeneSys ESS, Quadstar 422).

158   The chemical formula was calculated by an iterative approach. As a first step, the charges of

159 cations in tetrahedral, octahedral and interlayer sites were set equal to 22. The determined

160 composition of the anion site, populated by OH, F and O, was a result of this step. Given X = 2-

161 (OH+F), the chemical formula was thus calculated assuming 22+X positive charges for tetrahedral,

162 interlayer and octahedral sites, which leads to an assessment of anion composition and therefore to a

163 value for X. The iterative procedure was used until the difference in the X value from each step,

164 was $< 10^{-7}$ in magnitude.

165

7

166   *Single crystal X-ray diffraction*

167   Small crystal fragments of each sample, optically homogeneous and inclusion-free, were hand-

168   picked from the bulk sample and then analyzed using a Bruker X8 APEX four circle diffractometer

169   combined with an APEX 4K CCD detector, flat graphite monochromator and Mo Kα-radiation (λ =

170   0.7107 Å) from a fine focus sealed tube.   Data were processed using SAINT Plus (Bruker 2003).

171   The SADABS package (Sheldrick 1996) was used to perform a semi-empirical absorption

172   correction. Space group determination and data merging were performed using XPREP (Sheldrick,

173   1997). The crystal structure was refined by the SHELX-97 package of programs (Sheldrick, 1997).

174   Table 2 reports refined cell-parameters and other crystal data. Tables 3a and 3b list selected

175   interatomic distances and parameters obtained from the structure refinement for crystals showing

176   *C*2/*m* and *C*2 symmetry, respectively.   The mean electron counts for the octahedral and interlayer

177   sites, determined following the crystal structure refinement and electron microprobe analyses, are

178   listed in Table 1. Atom coordinates, equivalent and anisotropic displacement factors are reported in

179   Table 4[1].

180

181   *X-ray Absorption Spectroscopy (XAS)*

182   Fe *K*-edge XAS spectra were collected at the ESRF European Synchrotron Radiation Facilities

183   (ESRF, Grenoble, France) at the beamline BM-25 (Spanish Beamline, SpLine, Branch A). The

184   storage ring conditions were 6 GeV working in the current range 180-200 mA. A Si(111) double-

185   crystal monochromator was used, providing an energy resolution of ~ 0.4 eV at the Fe *K*-edge,

186   which is much less than the Fe *K* natural line width (~ 1.15 eV; Krause and Oliver 1979). A

187   metallic Fe foil was used as reference for energy calibration (energy reproducibility: ± 0.05 eV).

---

[1]For a copy of Table 4, deposit item AM-xx-yyy, contact the Business Office of the Mineralogical Society of America (see inside front cover of recent issue for price information). Deposit items may also be available on the American Mineralogist web at http://www.minsocam.org.

188   Data were collected on powder-pressed disks, made of an appropriate mixture of sample and

189   cellulose, in fluorescence mode at room conditions. Spectra were recorded over a range of 500 eV

190   across the Fe absorption K-edge with a 1 eV energy step in the edge region (7100-7150 eV) and a 3

191   eV energy steps in the Extended X-ray Absorption Fine Structure (EXAFS) region (7150-7500 eV).

192   Data from phlogopite, containing only a small amount of Fe^{2+} in the M1 site, annite characterized

193   by a full occupancy of Fe^{2+} in all the octahedral sites, and tetra-ferriphlogopite characterized by

194   Fe^{3+} for Si tetrahedral substitution were also collected as additional standards, and the results

195   compared to those of Giuli et al. (2001) and Tombolini et al. (2002). Standards analyzed were

196   chosen because of their similarity in topology to the samples under study and because of the

197   different iron oxidation and distribution within the layer.

198

199   *Site population*

200   The site preferences and site populations were assigned on the basis of: 1) the refined site-scattering

201   values (Table 1); 2) the unit formulae derived from the chemical compositions (Table 1); 3) the

202   observed bond-lengths (Table 3a, 3b); 4) the constraint to all sites, except M1, to be fully occupied;

203   5) the $^{[vi]}Fe^{3+}$ and $^{[vi]}Ti^{4+}$ occupancies constrained to the M1 and M2 site, respectively, following

204   Cesare et al. (2003); and 6) the electronic neutrality of the resulting formulae. The results are

205   reported in Table 5.

206

207   *Magnetic measurements*

208   Measurements of magnetic susceptibility were made on the six powder samples considered in a

209   temperature range of 2.2 - 300 K. Experiments were performed using a Quantum Design PPMS-7T

210   cryomagnetic system. Magnetic measurements were performed using a disk (about 10 mm in

211   diameter and 0.5 mm thick) prepared by a die-press of 36 mg of powdered mica crystals.

9

212   AC susceptibility (χ) was performed in the magnetic field of 10 Oe in field cooling mode. For

213   the Tapira sample, AC susceptibility was performed also in the magnetic field of 5000 Oe, both in

214   zero field cooling and field cooled modes. Isothermal magnetization curves and thermal scans in

215   constant field were measured, and the temperature dependence of the susceptibility deduced.

216   Data were obtained with the magnetic field applied along the plane of the sheets and thus

217   perpendicularly to c*. No direction was specified within the plane since the samples were generally

218   composed of several thin crystals with their planes approximately parallel to each other.

219   Diamagnetic contributions to the susceptibility from the sample holder and the atom cores were

220   approximately 0.4×10^{-6} emu. Demagnetization effects were negligible. Molar magnetic

221   susceptibility χ ($\chi = C/T$) was expressed in emu mol^{-1}. In particular, C is the Curie constant

222    $\left(C = \dfrac{Ng^2\mu_B^2 S(S+1)}{3k_B} \right)$, where: N = number of iron atoms per cm^3; μ_B = Bohr magneton; g =

223   gyromagnetic ratio; S = spin angular momentum ($S = 5/2$ for Fe^{3+} and $S = 2$ for Fe^{2+}); k_B =

224   Boltzman constant. The number of iron atoms per cm^3 and the Curie constants are listed in Table 1.

225

226   **Results and Discussion**

227   *Crystal chemistry and XANES spectroscopy*

228   Based on X-ray diffraction (XRD) and chemical data, iron is present in two different oxidation

229   states (Fe^{2+}, Fe^{3+}) and coordination (iv and vi) in the 1M trioctahedral micas under study. Four of

230   the samples (Albano, Oquossoc, Bryant Pond, and Tapira) with octahedral Fe^{2+} content ranging

231   from 0.378 to 1.476 apfu ($0.158 > [vi][Fe^{2+}/(Fe^{2+}+Mg)] < 0.679$) belong to the phlogopite-annite join,

232   two of these micas (Oquossoc and Bryant Pond) are Mg-rich annite, and two (Albano and Tapira)

233   are Fe-rich phlogopite (Rieder et al. 1998). Sample Catalão, with [iv]Fe^{3+} content 0.898 apfu, is a

234   tetra-ferriphlogopite and sample Eurajoki is a Li-rich siderophyllite with octahedral Fe^{2+} and Li

10

235   content of 1.027 and 1.042 apfu, respectively. In Tapira ($^{[vi]}Fe^{3+}$ = 0.313 apfu), and Albano

236   ($^{[vi]}Fe^{3+}$=0.279 apfu) Fe^{3+} octahedral occupancy is also observed (Table 1).

237   Figure 1 shows how samples are classified in terms of *mgli* vs. *feal* parameters, as defined by

238   Tischendorf et al. (1999), i.e. *mgli* = (Mg - Li); *feal* = (Fe_{total} + Mn + Ti - $^{[vi]}Al$). In crystals of the

239   phlogopite-annite join, $^{[vi]}Al$ is zero in Tapira and 0.073 in Albano (Table 1), thus indicating that the

240   siderophyllite end-member content is low. Mg-rich annites Oquossoc ($^{[vi]}Al$ = 0.377) and Bryant

241   Pond ($^{[vi]}Al$ = 0.485) plot in the annite field near the siderophyllite boundary.

242   The main exchange mechanisms where Fe increases in layer content in addition to (i)

243    $^{[iv]}Fe^{3+[iv]}Al^{3+}_{-1}$, which defines the phlogopite to tetra-ferriphlogopite join, include: (ii) $^{[vi]}Fe^{2+[vi]}Mg_{-1}$

244   , which defines the phlogopite to annite join, and (iii) $^{[iv]}Si$ $^{[vi]}Li$ $^{[iv]}Al_{-1}$$^{[vi]}Fe^{2+}_{-1}$ which defines the

245   polylithionite to siderophyllite join. The full heterovalent exchange vectors are: (i) $^{[vi]}Fe^{3+}_{2}$

246      $^{[vi]}Mg^{2+}_{-3}$, (ii) $^{[vi]}(Mg, Fe)^{2+}_{-1}$ $^{[iv]}Si^{4+}_{-1}$ $^{[vi]}Fe^{3+}$ $^{[iv]}Al^{3+}$, and (iii) $^{[vi]}Fe^{2+}_{-1}$ $(OH)_{-1}$$^{[vi]}Fe^{3+}O_{-2}$. All

247   trioctahedral micas under investigation are the 1*M*polytype. The crystal structure refinements

248   indicate the space group *C*2/*m* for five samples (Albano, Oquossoc, Bryant Pond, Tapira, and

249   Catalão). Based on (Fe^{2+}+Li) ordering in the *trans*-M1 site and in one of the two *cis*-sites (M3), the

250   layer symmetry is reduced to space group *C*2 in sample Eurajoki. Variability in chemical

251   composition, in particular when concerning the $Fe^{2+}/(Fe^{2+}+Fe^{3+})$ ratio, is reflected by several

252   structural parameters relating both to the tetrahedral (T) and octahedral (M) sheets.

253   The $^{[iv]}Fe^{3+}$ for $^{[iv]}Si^{4+}$ substitution notably affects tetrahedral features. Catalão tetra-

254   ferriphlogopite is characterized by the greatest tetrahedral volume (T_{volume}=2.40 $Å^3$) and by the

255   lowest tetrahedral flattening angle (τ =109.94°), very close to the theoretical 109.47° value. These

256   results indicate that $^{[iv]}Fe^{3+}$ substitution produces a regular tetrahedral site with the tetrahedral cation

257   located at the center. The mean tetrahedral basal edge length is greater in tetra-ferriphlogopite ($\langle$O-

258   O$\rangle_{basal}$ = 2.725(3) Å) than in Fe-rich phlogopite ($\langle$O-O$\rangle_{basal}$ = 2.701(3) Å for Tapira and ($\langle$O-O$\rangle_{basal}$ =

259   2.700(3) Å for Albano) and Mg-rich annite samples ($\langle$O-O$\rangle_{basal}$ = 2.701(3) Å for Oquossoc and $\langle$O-

11

260   O⟩$_{basal}$ = 2.698(3) Å for Bryant Pond) (Table 3a). The mean tetrahedral basal edge is approximately

261   related to the octahedral edge (i.e. average ⟨O3-O3⟩ distance) by the following relationship:

262    $\cos\alpha = \dfrac{\sqrt{3}}{2} \times \dfrac{\langle O3 - O3 \rangle}{\langle O - O \rangle_{basal}}$ (Brigatti and Guggenheim 2002), where α is the tetrahedral rotation

263   angle. Both the ⟨O3-O3⟩ octahedral mean edge distance and α increase following $^{[iv]}Fe^{3+}$ for $^{[iv]}Si$

264   substitution, thus indicating that $^{[iv]}Fe^{3+}$also produces a significantly greater tetrahedral ring

265   distortion (α in tetra-ferriphlogopite = 10.59°). The tetrahedral ring distortion significantly affects

266   interlayer coordination and the separation between two adjacent layers. In particular, ECoN

267   (effective coordination number, Weiss et al. 1992) of tetra-ferriphlogopite is 8.87° and the

268   interlayer separation is 3.463Å, which represent the lowest and the greatest value, respectively in

269   the considered dataset (Table 3a).

270   Octahedral mean bond distances (Table 3a) together with the scattering efficiencies (m.e.c.,

271   Table 1) indicate disorder of octahedral cation for samples Tapira, Albano and Catalão with m.e.c.

272   M1 ≈ m.e.c. M2 and mean bond distances ⟨M1-O⟩ ≈ ⟨M2-O⟩. For increasing $^{[vi]}Fe_{tot}/^{[vi]}(Fe_{tot}+Mg)$

273   ratios, Mg-rich annites Oquossoc and Bryant Pond display meso-octahedral ordering with m.e.c.

274   M1> m.e.c. M2 and ⟨M1-O⟩ > ⟨M2-O⟩.

275   The mean electron count determined for M1, M2, and M3 sites in the Eurajoki sample is M3 <

276   M1 < M2 (Table 1), whereas mean bond distances for two octahedral sites are similar (⟨M1-O⟩ ≈

277   ⟨M3-O⟩) and greater than values observed for the remaining site (⟨M2-O⟩) (Table 3b). Al

278   preferentially occupies the M2 site, whereas Fe and Li are disordered between M1 and M3 sites

279   with a slight preference of Fe for the M1 site.

280   Figure 2 shows the XANES Fe *K*-edge spectra of all the trioctahedral micas considered.

281   Phlogopite shows Fe^{2+} cations highly diluted among Mg atoms and, most probably, located in the

282   M1 site only. Like phlogopite, tetra-ferriphlogopite shows a limited amount of Fe in octahedral

12

283   coordination and Fe^{3+} mostly in tetrahedral coordination. Annite has Fe^{2+} completely disordered

284   over the entire octahedral sheet in all octahedral sites.

285   The pre-edge feature of tetra-ferriphlogopite (feature A, Figure 2a), attributed to the Fe^{3+} in

286   tetrahedral coordination (Dyar et al. 2001), is evident in sample Catalão at 7115.52 eV. Fe^{3+} is also

287   present, but less evident, in sample Tapira at 7116.72 eV. Feature A, is negligible in other samples,

288   thus suggesting that Fe^{3+} for samples Albano, Oquossoc, and Eurajoki can be assigned to octahedral

289   coordination only (Waychunas et al. 1983; Wilke et al. 2001).

290   The position of the threshold structure at 7127.2 eV in tetra-ferriphlogopite (feature B) is

291   consistent with Fe^{3+}. This feature is also present in samples Catalão, Tapira, Albano, Oquossoc and

292   Eurajoki. As suggested by Tombolini et al. (2002) the absorption edge position appears to follow

293   the $Fe^{3+}/(Fe^{3+}+Fe^{2+})$ ratio almost independently from the total iron content (Figure 2b).

294   The Fe^{2+} distribution in the octahedral sites is derived from the comparison of C, D, and E

295   features in phlogopite and annite. The intensity ratio between C and D effects suggests that samples

296   Oquossoc and Bryant Pond have the highest Fe/(Fe+Mg) ratio, whereas samples Tapira and Albano

297   have the lowest. Feature E can be related to Fe^{2+} ordering in octahedral sites (Tombolini et al.

298   2002). This feature occurs at 7141.6 eV and at 7144.5 eV in phlogopite and annite, respectively.

299   Feature E is in the range between 7144.4 eV (sample Oquossoc) and 7145.3 eV (sample Eurajoki)

300   thus suggesting that Fe is distributed in all octahedral sites. For sample Catalão, the Fe *K*-edge

301   XANES spectrum is similar to the spectrum of the standard tetra-ferriphlogopite, and shows high

302   complexity of the edge region. This pattern consists of several feature up to 20 eV above the edge

303   inflection at 7131.57 eV, and by a less well defined series of broad multiple scattering contributions

304   in the XANES region. This behavior is related to Fe structural disorder (i.e. Fe^{2+} and Fe^{3+} in the 2:1

305   layer in both tetrahedral and octahedral coordination), and results in a great number of Fe-O

306   distances to produce a XANES spectrum with broad features owing to the overlapping of multiple

307   scattering contributions (Tombolini et al. 2002).

13

308 *Magnetic behavior*

309 Fe is the main magnetic element in all samples under study (Table 1) and where present in

310 octahedral coordination, the magnetic interaction is super-exchange. This interaction occurs if Fe

311 atoms occupy two neighboring octahedral sites, and its sign depends on the angle defined by the

312 bonds of the two Fe cations with their shared oxygen atoms: weakly positive super-exchange

313 interaction is observed if the angle is near 90°, whereas negative super-exchange interaction is

314 observed if the angle is near 180° (Coey 1988; Coey and Ghose 1988). In samples under study,

315 relevant bond angles range from 91.5° to 121.4°. The lowest angle is observed in the Eurajoki Li-

316 rich siderophyllite, with a significant Fe^{2+} content present in two octahedral sites (i.e. M1 and M3,

317 with some Fe^{3+}in M2). The highest value is observed in the Bryant Pond Mg-rich annite, with a

318 homogeneous Fe^{2+} distribution in the three octahedral sites. Angles defined by apical oxygen atoms

319 with adjacent tetrahedral and octahedral cations are close to or >120°. Similarly, the angle defined

320 by adjacent tetrahedral cation with their shared basal oxygen atom is near 120°.

321 Bryant Pond and Oquossoc Mg-rich annite samples show maxima in the low field magnetic

322 susceptibility (χ) at 5.5 and 6.3 K, respectively. Following literature results (Coey 1988; Rancourt

323 et al. 1994; Pini et al. 2012), this result suggest an incipient antiferromagnetic ordering at low

324 temperature (Figures 3a, 3b). The Weiss θ constant, determined by extrapolation of the best fit

325 intercept of the $1/\chi$ curve with horizontal axis is 19 K and 13 Kfor Bryant Pond and Oquossoc

326 samples, respectively, thus suggesting a predominant ferromagnetic interaction (Figures 4a, 4b).

327 The positive value of the Weiss θ constant is consistent with the trends of $\chi \times T$-vs-T curves because

328 they plot above the constant values calculated at $\theta = 0$ and define trends typical for $\theta > 0$ values.

329 The $\chi \times T$ product increases with decreasing temperature, down to the values where the magnetic

330 ordering occurs (Figures 5a, 5b).

14

331   These results agree with the model of Coey et al. (1981) who studied the magnetic structure of

332   phyllosilicates. The model suggests that Fe atoms of the octahedral sheet are strongly coupled

333   within the plane by super-exchange ferromagnetic interactions. The magnetic interactions arising

334   from the plane with other octahedral sheets are weaker dipole-dipole interactions with dominant

335   antiferromagnetic character.

336   Figure 6 displays real and imaginary component of susceptibility as a function of temperature

337   for different frequencies for Bryant Pond sample. The dependency of the temperature of the peak

338   from the frequency of the applied magnetic field is consistent with a spin glass behavior. Further

339   evidence of spin grass is derived from the imaginary component trend that shows the inflection

340   point, corresponding to freezing temperature, moving to lower temperature values when decreasing

341   frequency of the applied magnetic field (Petracic et al. 2006). Spin glass involves short range

342   magnetic ordering below a given freezing temperature, where spins are frozen at random

343   orientations. The resulting system is different from a disordered pattern, observed at higher

344   temperature values, where the material shows paramagnetic behavior and clearly shows a

345   cooperative phenomenon.

346   Figure 7 reports the magnetization curves as a function of an increasing magnetic field H at a

347   constant temperature of 2.2K. For both Mg-rich annites, experimental values plot below their

348   theoretical Brillouin curves, thus suggesting that saturation is not reached under the effect of

349   significantly strong magnetic fields (7×10^4 Oe).

350   The low-field susceptibility of the Albano (Figures 3c, 4c, 5c) and Tapira (Figures 3d, 5d) Fe

351   rich-phlogopite samples were characterized at magnetic fields of 10 Oe by cooling from room

352   temperature to 2 K. High-field susceptibility was measured for sample Tapira, also at the

353   magnetic field of 5000Oe both in field cooling and field warming mode (Figure 8). Trends

354   obtained at H=5000 Oe for sample Tapira do not shows appreciable differences in behavior between

15

355   the two Fe-rich phlogopites (both at H=5000) and between sample Albano at H =10 and H=5000

356   Oe. The Weiss constant θ values are 4.4K and 5.2K for Albano and Tapira, respectively. These

357   values are lower than those previously calculated for Mg-rich annites. Different behavior is

358   observed between the two samples at a magnetic field of 10 Oe. Sample Tapira shows a peak at a T

359   ≅120K (Figure 3d), i.e. a temperature relatively high if compared to magnetic ordering temperatures

360   commonly observed for silicates (<100K). An effect at a much lower temperature (i.e. 2.4 K,

361   Figure 3d) is also identified. This latter effect, unlike the one observed at 120K, can be observed if

362   increasing magnetic intensity to ≤5000 Oe. The lack of the effect at higher temperature, when

363   increasing magnetic intensity, is related to small Fe oxide inclusions in the Tapira sample, as

364   demonstrated by microprobe analysis and by calorimetric analysis.

365   Sample Tapira shows in the temperature range from 100 to 140K, a regular decrease in heat

366   capacity without displaying the variation in slope commonly observed for this and for other samples

367   at lower temperatures, in correspondence with their peak in magnetic susceptibility. This behavior

368   is consistent with a magnetic transition affecting a small portion of the crystal that does not affect

369   thermal capacity. Fe oxides, such as magnetite, undergoes a well-defined magnetic transition at T

370   ≅120 K (Verwey magnetic transition, Gridin et al. 1996; Tarnawsky et al. 2004; Tabiśet al. 2007).

371   This mechanism is consistent with the oxidation process described by Rancourt et al. (2001) and

372   Dunlop et al. (2006) for micas originating at higher oxygen fugacity values. Thus the mechanism is

373   consistent with the petrogenetic processes accepted for the Tapira complex.

374   In tetra-ferriphlogopite (Catalão), χ variation versus temperature defines the trend commonly

375   observed for paramagnetic materials (Figure 3e). The curve χ×T plots below the theoretical value

376   for the sample composition, at θ=0, thus suggesting that the magnetic interaction among Fe atoms is

377   mostly anti-ferromagnetic (Figure 5e). This result also matches the trend of the 1/χcurve (Figure

378   4d) that defines a negative value for Weiss θ constant (≈-25 K). This behavior is consistent with

16

379   super-exchange that describes Fe^{3+}-O-Fe^{3+} as negative (i.e. antiferromagnetic) and with literature

380   data (e.g., Coey, 1981). The magnetization curve for the Catalão sample shows a lower increase in

381   magnetization at increasing magnetic field, when compared to other samples and remarkably lower

382   values at high values of an applied magnetic field (Figure 7). This behavior is related to the

383   interaction of Fe cations in octahedral coordination, only in M1, with Fe cations in tetrahedral

384   coordination, and to interactions among tetrahedral Fe cations. The different behavior of this

385   sample, is related to the different oxidation state of the Fe atoms involved in the interaction (i.e.

386   Fe^{3+} vs. Fe^{2+}) and to their coordination (tetrahedral and octahedral). The bond angles defined by

387   two adjacent Fe cations with their shared octahedral oxygen atoms is near 120°. Similarly two

388   adjacent tetrahedral cations define with their shared basal oxygen atoms angles near 120^0. The

389   interaction inside the tetrahedral sheet is however extremely unlikely to occur, if considering charge

390   balance of the bridging basal oxygen atoms. In contrast, the interaction among tetrahedral and

391   octahedral sites are confined to the atoms inside the layer, because two adjacent layers are separated

392   by the non-magnetic interlayer cations.

393   Li-rich siderophyllite Eurajoki sample shows a peak in χ at higher temperatures than observed

394   for other samples (i.e. 7.6 K), possibly as a consequence of uniform Fe distribution among the

395   octahedral sites with Fe^{2+} mostly located in M1 and M3 sites and Fe^{3+} in M2 site (Figure 3f). This

396   sample shows magnetic interactions that are predominantly ferromagnetic within the layers. The

397   inverse of χ approximates the Curie law and defines a θ constant of 17K (Figure 4e). Similarly to

398   other samples, the $\chi \times T$ curve plots above the theoretical value characterizing $\theta = 0$ for sample

399   composition (Figure 5f).

400

401   **Concluding remarks and implications.**

402   Reported data detail magnetic properties for micas with different Fe content, different Fe

403   coordination, and different Fe oxidation state. Total Fe content is not able to account for the

17

404   observed magnetic properties of the studied micas. Some samples (e.g., Oquossoc, Bryant Pond)

405   show for T < 10 K similar magnetic effects: i.e. maxima in magnetic susceptibility and similar

406   variation in $\chi \times T$–vs–T. In contrast, the Albano sample does not show any maximum in magnetic

407   susceptibility, despite intermediate Fe content, at low temperature, which is the trend commonly

408   observed for paramagnetic materials. Different magnetic behavior is thus better explained by

409   considering the Fe crystal chemistry, such as distribution of Fe among octahedral and tetrahedral

410   sites and the $Fe^{2+}/(Fe^{2+}+Fe^{3+})$ ratio. Where Fe is mostly present in octahedral coordination,

411   dominant magnetic interactions among Fe atoms are ferromagnetic, which becomes stronger at high

412    $Fe^{2+}/(Fe^{2+}+Fe^{3+})$ ratio. Samples with high $Fe^{2+}/(Fe^{2+}+Fe^{3+})$ ratio are also characterized by high

413   values of Curie-Weiss θ (Bryant Pond θ = 19 K and Oquossoc θ = 13 K). Where $Fe^{2+}/(Fe^{3+}+ Fe^{2+})$

414   ratios decrease, the θ value also decreases. For sample Catalão showing predominant Fe^{3+} in

415   tetrahedral coordination, the sample shows predominant anti-ferromagnetic interactions with a

416   negative value of the Curie-Weiss θ constant (i.e. θ = - 25 K).

417   The data for micas suggest a spin-glass behavior, as indicated by the dependency of the

418   maxima in magnetic susceptibility from the frequency of the applied magnetic field. This result

419   differs from the long range magnetic ordering at low T reported by Coey et al.(1981), Beausoleil et

420   al. (1983) and Rancourt et al. (1994). This difference is related to Fe^{3+} content that, as suggested by

421   Ballet et al. (1985), can locally randomize the ferromagnetic ordering inside the plane, and to non-

422   ferromagnetic elements. This result is consistent with the lower Fe content, which is characterized

423   by the studied samples, when compared to those reported in the literature.

424   Figure 9 relates magnetic ordering, either antiferromagnetic planar long range order or spin

425   glass short range order, as a function of p33 (i.e. the probability that two Fe^{3+} cations are placed in

426   adjacent octahedra) and the total number of octahedral Fe cations per unit formula (Z). This plot

427   demonstrates that spin glass behavior is favored at low Z and high p33 values.

18

428   Both θ and Tm (i.e, the maximum susceptibility temperature) seem to linearly depend on the

429   number of Fe atoms in octahedral coordination per unit cell, Z (Figure 10, Table 6). Greater θ

430   values are however observed in a sample showing intermediate Z, thus suggesting an influence of a

431   lower than ideal symmetry and to the presence of Fe^{2+} ordering on M1 and M3 sites. This

432   distribution increases the probability of ferromagnetic interaction among two adjacent Fe^{2+} atoms.

433

442

19

References cited list

Anagnostopoulos, T., Calamiotou, M., and Sidzris, C. (1973) Magnetic behavior of some biotite
samples from west Thrace, N.E. Greece. Clays and Clay Minerals 21, 459-464.

Bailey, S.W. (1984) Crystal chemistry of the true micas. In Micas, S.W. Bailey Editor, Reviews in
Mineralogy, 13, 357-467.

Ballet,O. (1986) Comment on magnetism in biotites. Physics and Chemistry of Minerals, 13, 281.

Ballet, O., Coey, J.D.M., Mangin, P., and Townsend, M.G. (1985) Ferrous talc - a planar
antiferromagnet. Solid State Communications, 55, 787-790.

Ballet, O., and Coey, J.M.D. (1982) Magnetic properties of sheet silicates; 2:1 layer minerals.
Physics and Chemistry of Minerals, 8, 218-229.

Beausoleil, N., Lavallèe, P., Yelon, A., Ballet, O., and Coey, J.M.D. (1983) Magnetic properties of
biotite micas. Journal of Applied Physics, 54, 906-915.

Biedermann, A.R., Bender Koch C., Lorenz W.E.A., and Hirt A.M. (2014) Low-temperature
magnetic anisotropy in micas and chlorite. Tectonophysics, 629, 63-74.

Brigatti, M.F., and Guggenheim, S. (2002) Mica crystal chemistry and the influence of pressure,
temperature, and solid solution on atomistic models. In: Mottana, A., Sassi, F.P., Thompson,
J.B. Jr, Guggenheim, S. (eds) Micas: crystal chemistry and metamorphic petrology. Review in
Mineralogy and Geochemistry, 46, Mineralogical Society of America, Washington DC, 1-98.

Brigatti, M.F., Medici, L., Saccani, E., and Vaccaro, C. (1996) Crystal chemistry and petrologic
significance of Fe^{3+}-rich phlogopite from the Tapira carbonatite complex, Brazil.
AmericanMineralogst, 81, 913-927.

Brigatti, M.F., Caprilli, E., Funiciello, R., Giordano, G., Mottana, A., and Poppi, L. (2005) Crystal
chemistry of ferroanphlogopites from the Albano maar lake (Colli Albani Volcano, Central
Italy). European Journal of Mineralogy, 17, 611-621.

20

468   Brod, J.A., Gaspar, J.C., de Araújo, D.P., Gibson, S.A., Thompson, R.N., and Junqueira-Brod, T.C.

469   (2001) Phlogopite and tetra-ferriphlogopite from Brazilian carbonatite complexes: Petrogenetic

470   constraints and implications for mineral-chemistry systematics. Journal of Asian Earth

471   Sciences, 19, 265-296.

472   Bruker (2003) SMART and SAINT-Plus, version 6.01. Bruker AXS Inc., Madison, Wisconsin.

473   Catalli, K., Shim, S.H, Dera, P., Prakapenka, V.B., Zhao, J., Sturhahn, W., Chow, P., Xiao, Y.,

474   Cynn, H., and Evans, W.J. (2011) Effects of the Fe^{3+} spin transition on the properties of

475   aluminous perovskite – New insights for lower-mantle seismic heterogeneities. Earth and

476   Planetary Science Letters, 310, 293-302.

477   Cesare, B., Cruciani, G., and Russo, U. (2003) Hydrogen deficiency in Ti-rich biotite from anatectic

478   metapelites (El Joyazo, SE Spain): Crystal-chemical aspects and implications for high-

479   temperature petrogenesis. American Mineralogist, 88, 583-595.

480   Christie, I.A.D., Rancourt, D.G., Lamarche, G., Royer, M., Kodama, H., and Robert, J.-L. (1992)

481   Low temperature Mössbauer spectroscopy and magnetism of synthetic annite mica. Hyperfine

482   Interactions, 68, 315-318.

483   Coey, J.M.D. (1985) Magnetic order in trioctahedral sheet silicates: a review. Proceedings

484   International Clay Conference, Denver, 261-266.

485   Coey, J.M.D. (1987) New permanent magnet materials. Physica Scripta. T19B, 426-434.

486   Coey, J.M.D. (1988) Magnetic properties of iron in soil iron oxides and clay minerals. In J.W.

487   Stucki, B.A. Goodman, U. Schwertmann (Eds). Iron in soils and Clay Minerals. NATO ASI

488   Series, 217, pp 397-466.

489   Coey, J.M.D., and Ghose, S. (1988) Magnetic ordering and thermodynamics in silicates. NATO

490   ASI Series, Series C, Mathematical and Physical Sciences, 225, 459-499.

491   Coey, J.M.D., Ballet, O., Moukarika, A., and Soubeyroux, J.L. (1981) Magnetic properties of sheet

492   silicates; 1:1 layer minerals. Physics and Chemistry of Minerals, 7, 141-148.

21

493   Coey, J.M.D., Moukarika, A., and Ballet, O. (1982) Magnetic order in silicate minerals. Journal of

494   Applied Physics, 53, 8320-8325.

495   Coey, J.M.D., Chukhrov, F.V., and Zvyagin, B.B. (1984) Cation distribution, Mössbauer spectra,

496   and magnetic properties of ferri-pyrophyllite. Clays and Clay Minerals, 32, 198-204.

497   Donovan, J.J. (1995) PROBE: PC-based data acquisition and processing for electron microprobes.

498   Advanced Microbeam, 4217 King Graves Rd, Vienna, Ohio, 44473.

499   Dunlop, D.J., Özdemir, Ö., and Rancourt, D.G. (2006)Magnetism of biotite crystals. Earth and

500   Planetary Science Letters, 243, 805-819.

501   Dyar, M.D., Delaney, J.S., and Sutton, S.R. (2001) Fe XANES spectra of iron-rich micas.

502   European Journal of Mineralogy, 13, 1079-1098.

503   Foley, S.F. (1989) Experimental constraints on phlogopites chemistry in lamproites: 2. the effect of

504   pressure-temperature variations. European Journal of Mineralogy, 2, 327-341.

505   Giuli, G., Paris, E., Wu, Z.Y., Brigatti, M.F., Cibin, G., Mottana, A., and Marcelli, A. (2001)

506   Experimental and theoretical XANES and EXAFS study of tetra-ferriphlogopite. European

507   Journal of Mineralogy, 13, 1099-1108.

508   Guidotti, C.V., Cheney, J.T., and Henry, D.J. (1988) Compositional variation of biotite as a

509   function of metamorphic reactions and mineral assemblage in the pelitic schist of western

510   Maine. American Journal of Science, 288-A, 270-292

511   Gridin, V.V., Hearne, G.R., and Hoing, J.M. (1996) Magnetoresistance extremum at the first-order

512   Verwey transition in magnetite (Fe_3O_4). Physics Review B, 53, 15518-15521.

513   Haapala, I. (1977) Petrography and geochemistry of the Eurajoki stock, a Rapakivi-granite complex

514   with greisen-type mineralization in southwest Finland. Geological Survey of Finland Bulletin,

515   286.

22

516   Hsu, H., Umemoto, K., Blaha, P., and Wentzcovitch, R.M. (2010) Spin states and hyperfine

517   interactions of iron in (Mg, Fe)SiO$_3$perovskite under pressure. Earth and Planetary Science

518   Letters, 294, 19-26.

519   Krause, M.O., and Oliver, J.H. (1979) Natural widths of atomic K and L Levels, Kα X-Ray lines

520   and several KLL Auger lines. Journal of Physical and Chemical Reference Data 8, 329-338.

521   Laurora, A., Malferrari, D., Brigatti, M. F., Mottana, A., Caprilli, E., Giordano, G., and Funiciello,

522   R. (2009) Crystal chemistry of trioctahedral micas in the top sequences of the ColliAlbani

523   volcano, Roman Region, Central Italy. Lithos 113, 507-520.

524   Longworth, G., Townsend, M.G., Provencher, R., and Kodama, H. (1987) Magnetic interaction in

525   biotites and oxidisedbiotites. Physics and Chemistry of Minerals 15, 71–77.

526   Marcelli, A., Cibin, G., Di Matteo, S., Chaboy, J., Di Gioacchino, D., Tripodi, P., Brigatti, M.F.,

527   and Mottana, A. (2004) Octahedral low spin symmetric configurations vs. high spin octahedral

528   distorted configurations: the case of Fe in natural layered silicates. Journal of Physics and

529   Chemistry of Solids, 65, 1491-1500.

530   Meyrowitz, R. (1970) New semi-micro-procedure for determination of ferrous iron in refractory

531   silicate minerals using a sodium metafluoborate decomposition. Analytical Chemistry, 42,

532   1110-1113.

533   Petracic, O., Chen, X., Bedanta, S., Kleemann, W., Sahoo, S., Cardoso, S., and Freitas P.P. (2006)

534   Collective states of interacting ferromagnetic nanoparticles. Journal of Magnetism and

535   Magnetic Materials, 300, 192-197.

536   Pini, S., Brigatti, M.F., and Affronte, M. (2008) Magnetic behaviour of trioctahedral mica-2M1

537   occurring in a magnetic anomaly zone. Mineralogical Magazine, 72, 1035-1042.

538   Pini, S., Brigatti, M.F., Affronte, M., Malferrari, D., and Marcelli, A. (2012) Magnetic behavior of

539   trioctahedral micas with different octahedral Fe ordering. Physics and Chemistry of Minerals,

540   39, 665-674.

23

541   Rancourt, D.G., Christie, I.A.D., Lamarche, G., Swainson, I., and Flandrois, S. (1994) Magnetism

542   of synthetic and natural annite mica: ground state and nature of excitations in an exchange-wise

543   two-dimensional easy-plane ferromagnet with disorder. Journal of Magnetism and Magnetic

544   Materials, 138, 31-44.

545   Rancourt, D.G., Mercier, P.H.J., Cherniak, D.J., Desgreniers, S., Kodama, H., Robert, J.-L., and

546   Murad, E. (2001) Mechanisms and crystal chemistry of oxidation in annite: resolving the

547   hydrogen-loss and vacancy reactions. Clays and Clay Minerals, 49, 455-491.

548   Redhammer, G.J., Senyshyn, A., Tippelt, G., and Roth, G. (2011) Magnetic spin structure of

549   pyroxene-type $MnGeO_3$. Journal of Physics: Condensed Matter, 23, 254202-254213.

550   Redhammer, G.J., Senyshyn, A.,Tippelt, G.,Pietzonka, C.,Treutmann, W.,Roth, G., and

551   Amthauer,G. (2012) Magnetic and low-temperature structural behavior of clinopyroxene-type

552        $FeGeO_3$: A neutron diffraction, magnetic susceptibility, and ^{57}Fe Mössbauer study. American

553   Mineralogist, 97, 694-706.

554   Rieder, M., Cavazzini, G, D′yakonov, Y.S., Frank-Kamenetskii, V.A., Gottardi, G., Guggenheim,

555   S., Koval, P.V., Müller, G., Neiva, A.M.R., Radoslovich, E.W., Robert, J.-L., Sassi, F.P.,

556   Takeda, H., Weiss, Z., and Wones, D.R. (1998) Nomenclature of the micas. Clays and Clay

557   Minerals, 41, 61-72.

558   Sheldrick, G.M. (1996) SADABS. University of Göttingen, Germany.

559   Sheldrick, G.M. (1997) SHELX-97, program for crystal structure determination. University of

560   Göttingen, Germany.

561   Tabiś, W., Tarnawski, Z., Kąkol, Z., Król, G., Kołodziejczyk, A., Kozłowski, A., Fluerasu, A., and

562   Honig, J.M. (2007) Magnetic and structural studies of magnetite at the Verwey transition.

563   Journal of Alloys and Compounds, 442, 203-205.

24

564   Tarnawski, Z., Wiechec, A., Madej, M., Nowak, D., Owoc, D., Król, G., Kąkol, Z., Kolwicz-

565   Chodak, L., Kozlowsi, A., and Dawid, T. (2004) Studies of the Verwey transition in magnetite.

566   Acta Physica Polonica A, 106, 771-775.

567   Tischendorf, G., Förster, H.-J., and Gottesmann, B. (1999) The correlation between lithium and

568   magnesium in trioctahedral micas: Improved equations for Li_2O estimation from MgO data.

569   Mineralogical Magazine, 63, 57-74.

570   Tombolini, F, Marcelli, A., Mottana, A., Cibin, G., Brigatti, M.F., and Giuli, G. (2002) Crystal

571   chemical study by XANES of trioctahedral micas: the most characteristic layer silicates.

572   International Journal of Modern Physics B, 16, 1673-1679.

573   Townsend, M.G. (1987) 'Comment on magnetism in biotites' by O. Ballet. Replay. Physics

574   Chemistry of Minerals, 13, 282-283.

575   Townsend, M.G., and Longworth, G. (1985) Sign of the magnetic coupling of iron (2+) and iron

576   (3+) ions in biotite. Physics and Chemistry f Minerals, 12, 141–144.

577   Townsend, M.G., Longworth, G., Ross, C.A.M., and Provencher, R. (1987) Ferromagnetic or

578   antiferromagnetic iron III spin configurations in sheet silicates. Physics Chemistry of

579   Minerals,15, 64-70.

580   Waychunas, G.A., Apted, M.J., and Brown, G.E. Jr (1983) X-ray K-edge absorption spectra of Fe

581   minerals and model compounds: near edge structure. Physics Chemistry of Minerals, 10, 1-9.

582   Weiss, Z., Rieder, M., and Chmielovà, M. (1992) Deformation of coordination polyhedra and their

583   sheets in phyllosilicates. European Journal of Mineralogy, 4, 665-682.

584   Wilke, M., Farges, F., Petit, P.E., Brown, G.E. Jr, and Martin, F. (2001) Oxidation state and

585   coordination of Fe in minerals: An Fe K-XANES spectroscopic study. American Mineralogist,

586   86, 714-730.

587

25

588   **List of figure captions**

589   Figure1. Micas on the classification diagram after Tischendorf et al. (1999). *mgli* = (Mg - Li); *feal*

590   = (Fe$_{Tot}$ + Mn + Ti - $^{[vi]}$Al). Symbols: circle = Bryant Pond; triangle down = Oquossoc;

591   hexagon = Tapira; diamond = Albano; triangle up: Catalão; square = Eurajoki.

592   Figure2.a) Fe *K*-edge XANES spectra of studied micas compared with phlogopite, tetra-

593   ferriphlogopite and annite. b) Comparison between the energy position of the threshold

594   structure of micas containing both Fe^{2+} and Fe^{3+} mainly in octahedral position.

595   Figure 3. Trend of the real (in-phase) component of the magnetic susceptibility (χ) vs. temperature,

596   measured at *H* =10 Oe in Field Cooling. a) Bryant Pond; b) Oquossoc; c) Albano; d) Tapira;

597   e) Catalão; f) Eurajoki.

598   Figure 4. Inverse of the real component of the magnetic susceptibility (1/χ) vs. temperature

599   measured at *H* =10 Oe in Field Cooling. The solid line represents the linear fit of the curve in

600   the region of temperature between 80 and 200 K, together with *r*^{2} values. a) Bryant Pond; b)

601   Oquossoc; c) Albano; d) Catalão; e) Eurajoki.

602   Figure 5. Temperature dependence of the product (χ×T). The solid line represents the theoretical

603   product $\chi \times T \approx \frac{1}{8} g^2 S (S + 1)$ where *g* is the gyromagnetic ratio and S the spin angular momentum

604   (*S* = 5/2 for Fe^{3+} and *S* = 2 for Fe^{2+}). a) Bryant Pond; b) Oquossoc; c) Albano; d) Tapira; e)

605   Catalão; f) Eurajoki.

606   Figure 6. Real χ (a) and the imaginary part χ′ (b) of the AC susceptibility as a function of

607   temperature and frequency.

608   Figure 7. Sample magnetization vs. magnetic field (H). Symbols: filled circles = Bryant Pond;

609   filled diamonds = Oquossoc; filled triangles up = Albano; filled squares = Catalão; filled

610   triangles down = Eurajoki; open triangles = Brillouin curve for Fe^{2+} (J=2); open squares =

611   Brillouin curve for Fe^{3+} (J=5/2). The Brillouin curve was defined as $M = M_S B_J(y)$ where M_S

                                                    26

612   represent the magnetization at the saturation point (referred to one mole) and calculated as

613 $M_S = N_A g \mu_B J$. N_A = Avogadro constant, g = gyromagnetic ratio, μ_B = Bohr magneton; J

614   = magnetic total angular momentum; $B_J(y)$ (i.e. the Brillouin function) =

615     $B_J(y) = \dfrac{2J+1}{2J} \coth(\dfrac{2J+1}{2J} y) - \dfrac{1}{2J} \coth \dfrac{y}{2J}$ where $y = g \mu_B J \dfrac{B}{k_B T}$.

616   Figure 8. Sample Tapira: a) In-phase susceptibility as a function of temperature with an applied

617   filed of 5000 Oe. Open symbol show susceptibility when cooling from room temperature

618   and crosses when warming from low temperature. b) $\chi \times T$ vs. temperature; the solid line

619   represents the theoretical product (for details see the footnote of Figure 5; c) Inverse of the in-

620   phase magnetic susceptibility ($1/\chi$) vs. temperature; the solid line represents the linear fit of

621   the curve in the region of temperature between 80 and 200K.

622   Figure 9. Magnetic behavior (spin-glass vs. long range magnetic ordering), as a function of Z

623   (octahedral Fe content) and *p33* representing the probability that two adjacent octahedral sites

624   are occupied by Fe^{3+} cations. Samples plotting to the left of the dashed line all present spin-

625   glass behavior, unlike samples plotting to the right that present long range magnetic ordering.

626   Filled symbols: this study (circle = Tapira, triangle up =Albano; triangle down = Oquossoc;

627   square: Bryant Pond; diamond = Catalão; hexagon = Eurajoki). Open symbols: samples from

628   literature (Ballet et al. 1985, Ballet and Coey 1982, Rancourt et al. 1994).

629   Figure 10. a) Curie-Weiss constant vs. Z (Fe cations in octahedral coordination); b) temperature of

630   maximum in magnetic susceptibility vs. the tetrahedral rotation angle α. Filled symbols: this

631   study (circle = Tapira, triangle up =Albano; triangle down = Oquossoc; square: Bryant Pond;

632   diamond = Catalão; hexagon = Eurajoki). Open symbols: samples from literature (Ballet et

633   al. 1985, Ballet and Coey 1982, Rancourt et al. 1994).
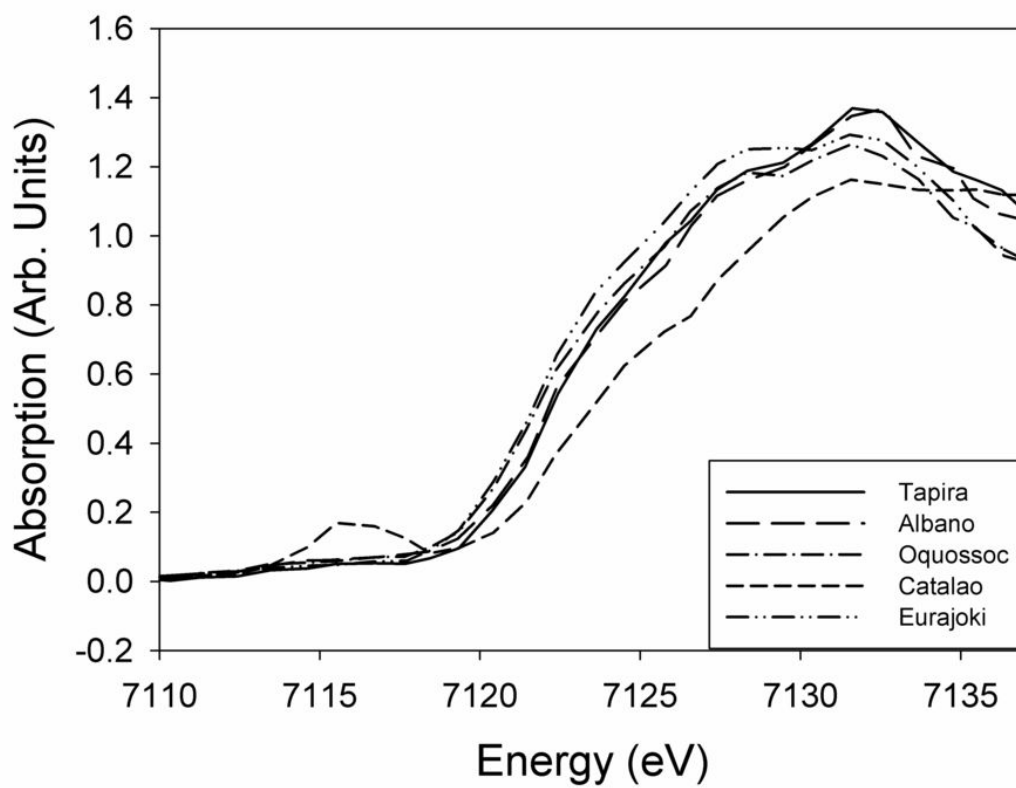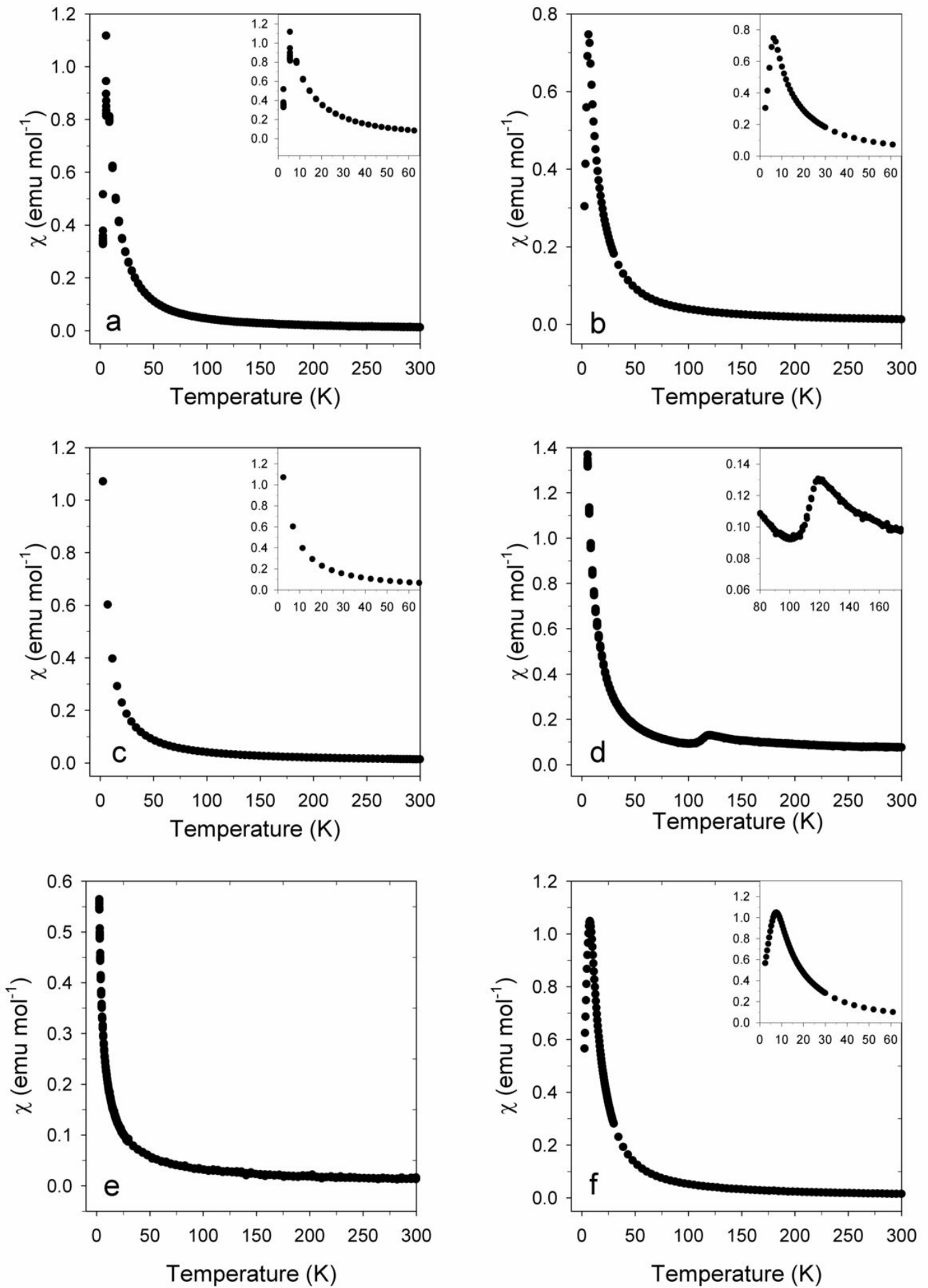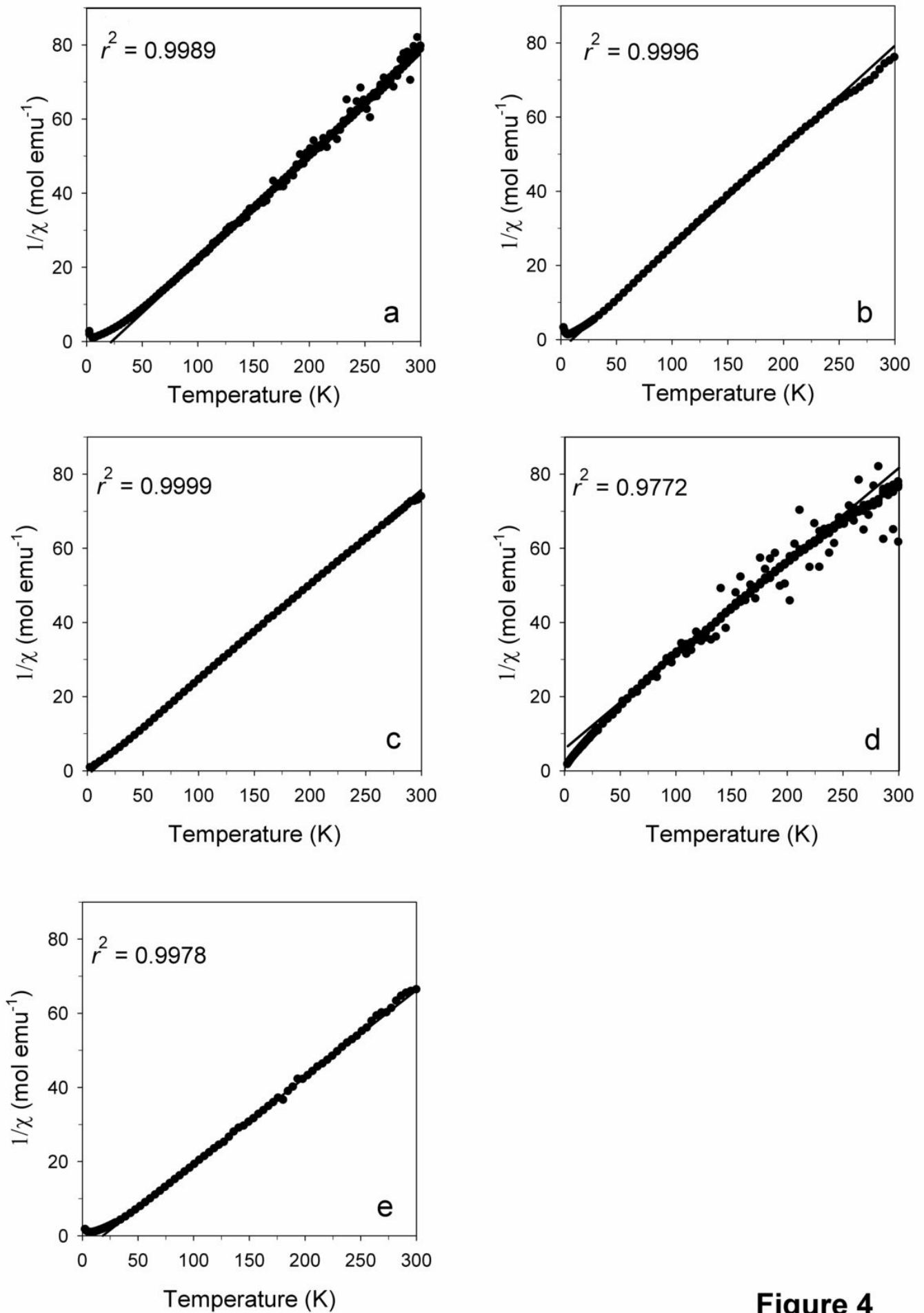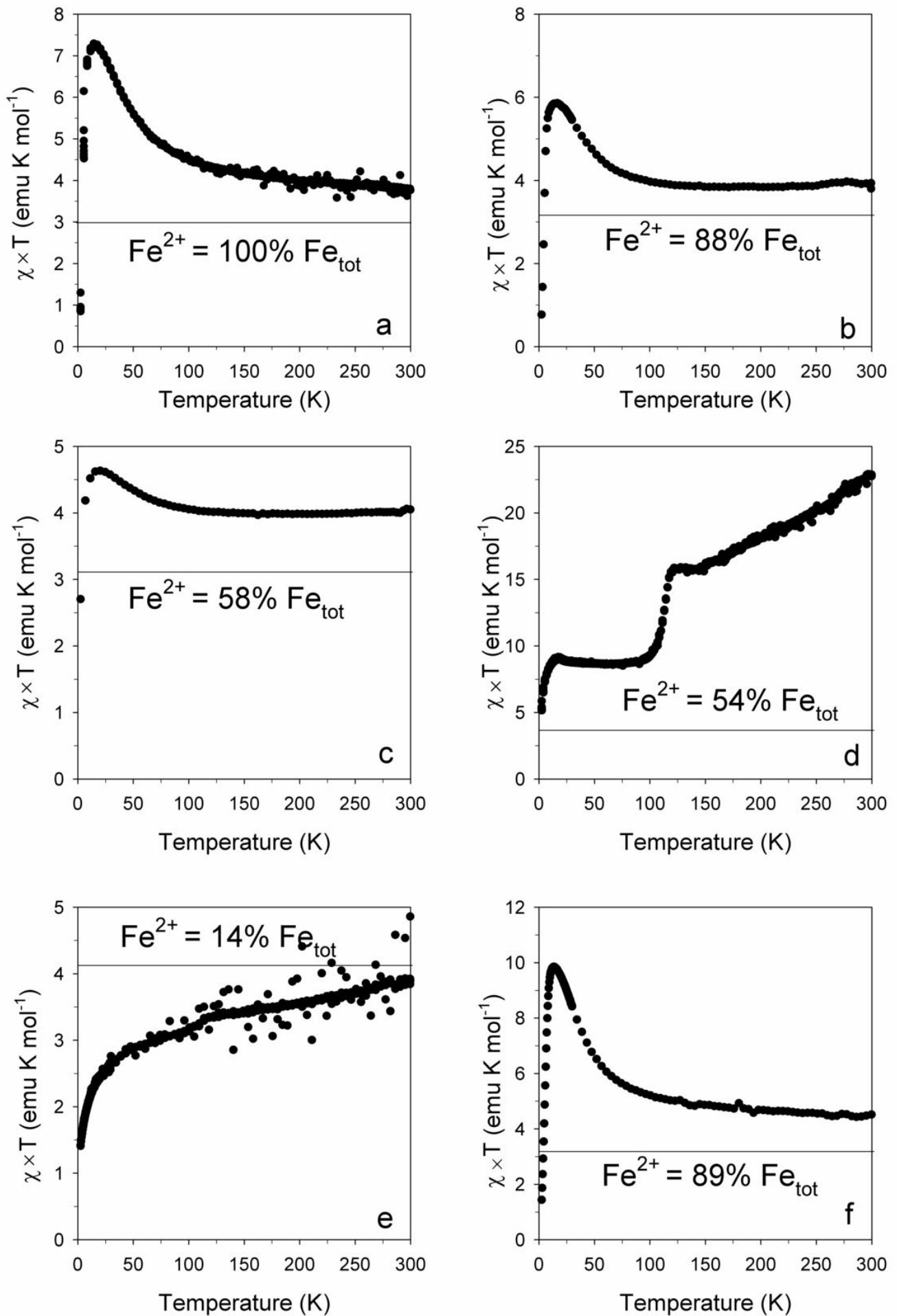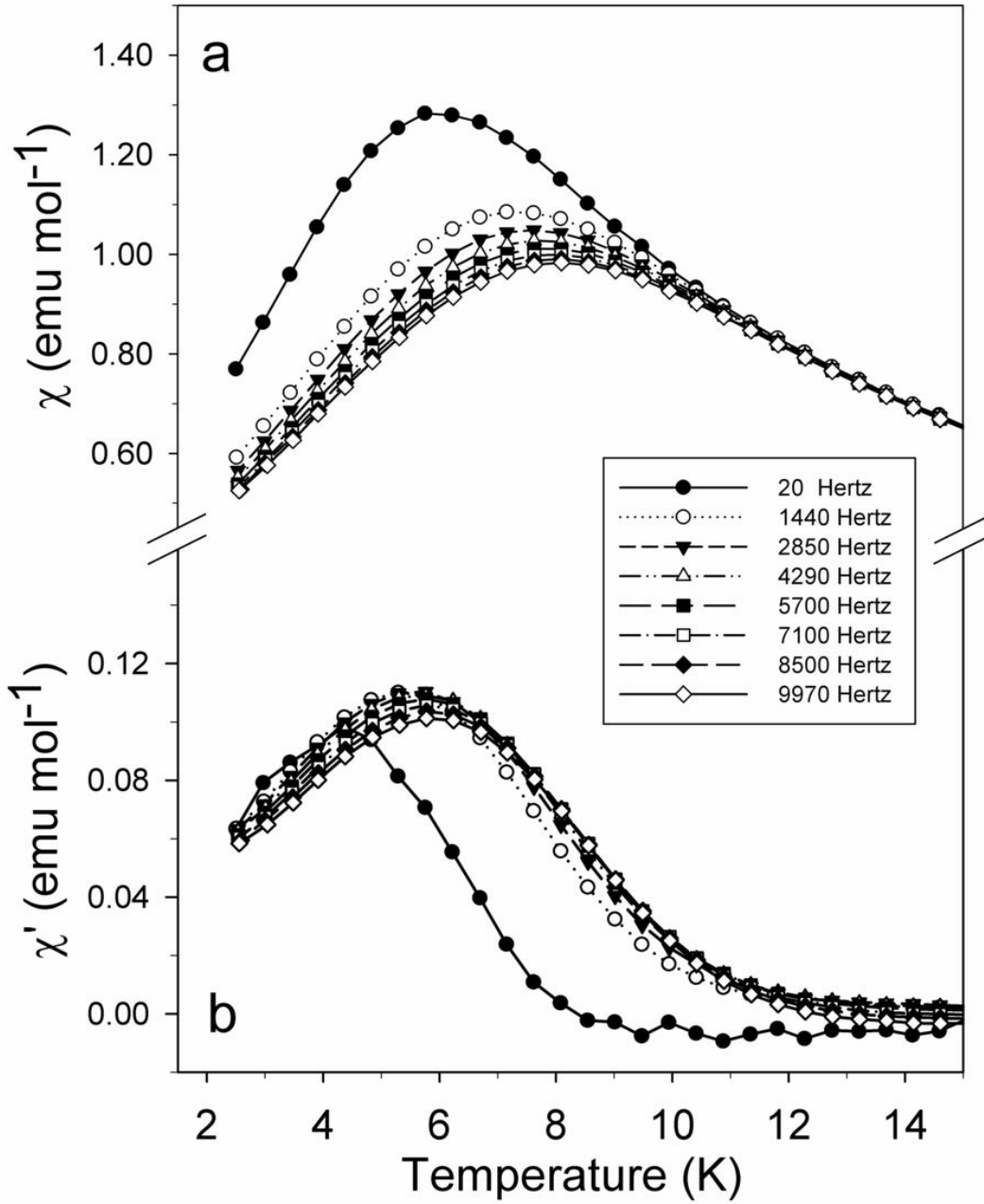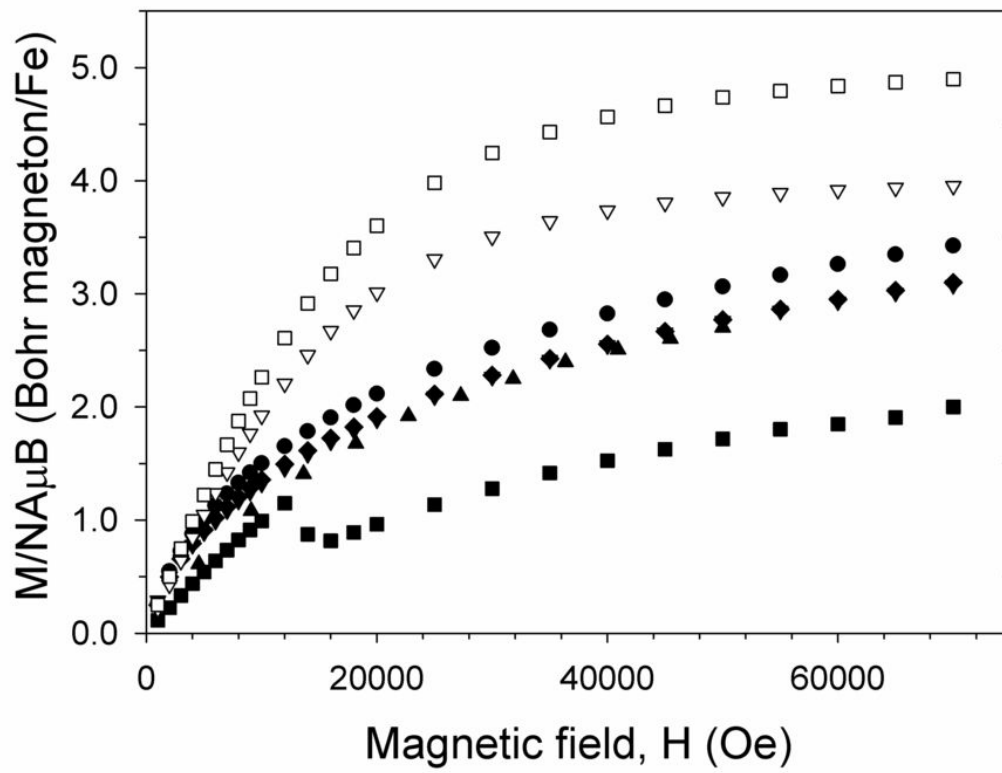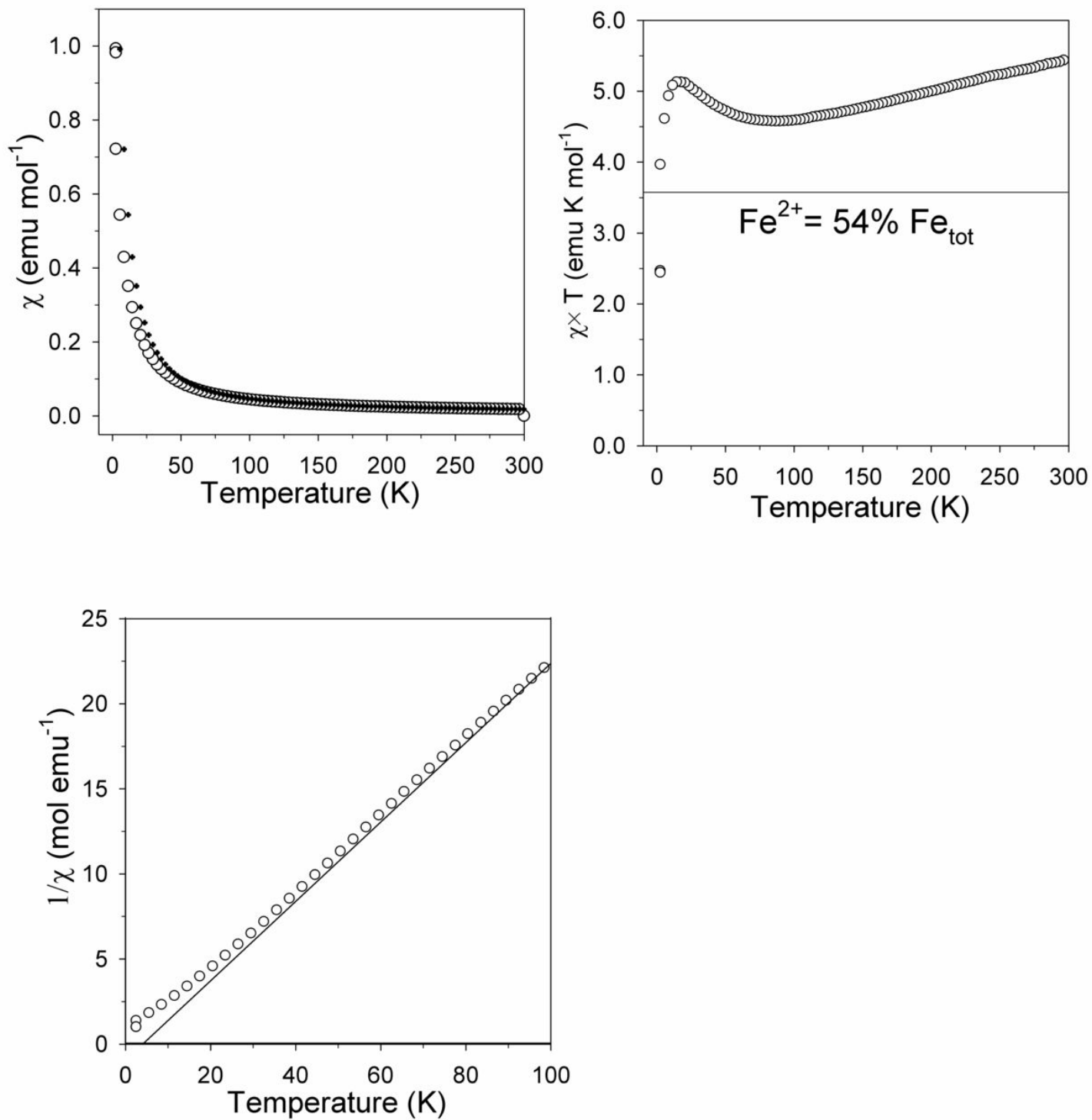
27
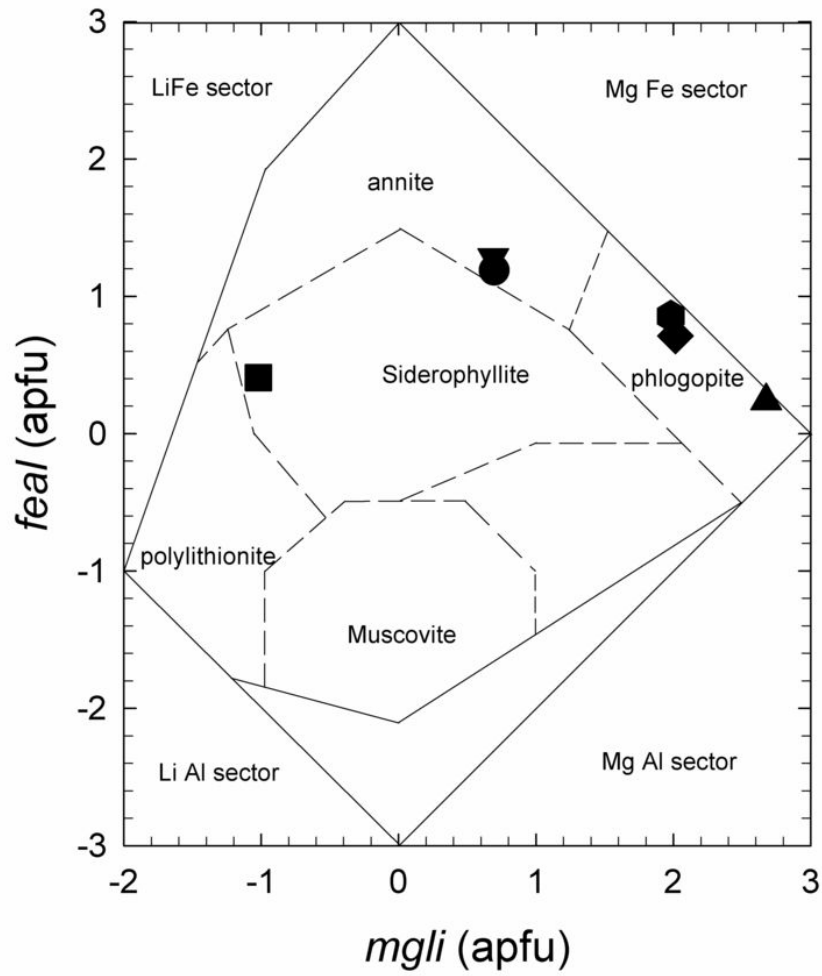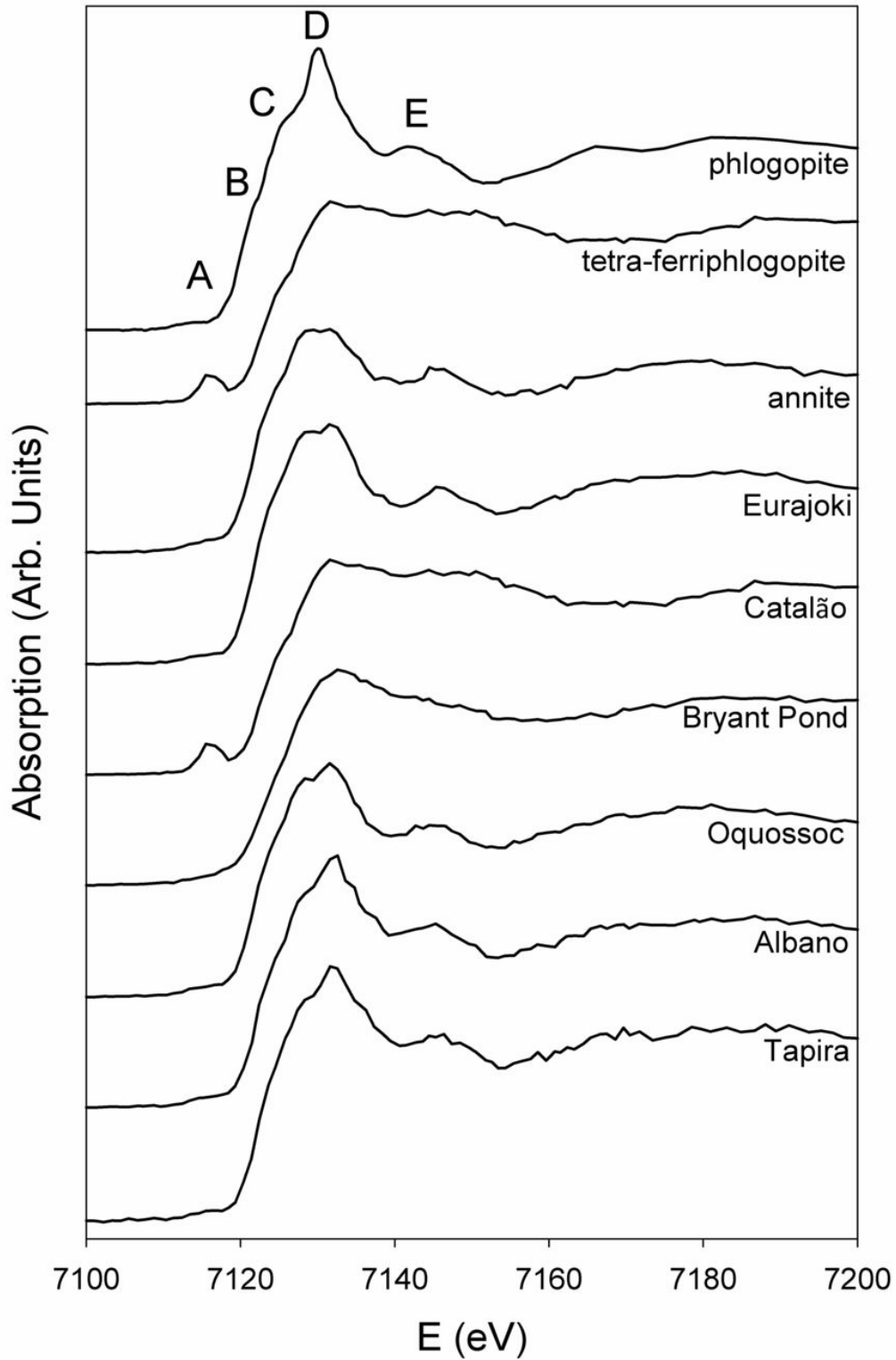
Figure 1

Figure 2a

Figure 2b

Figure 3

Figure 4

Figure 5

Figure 6

Figure 7
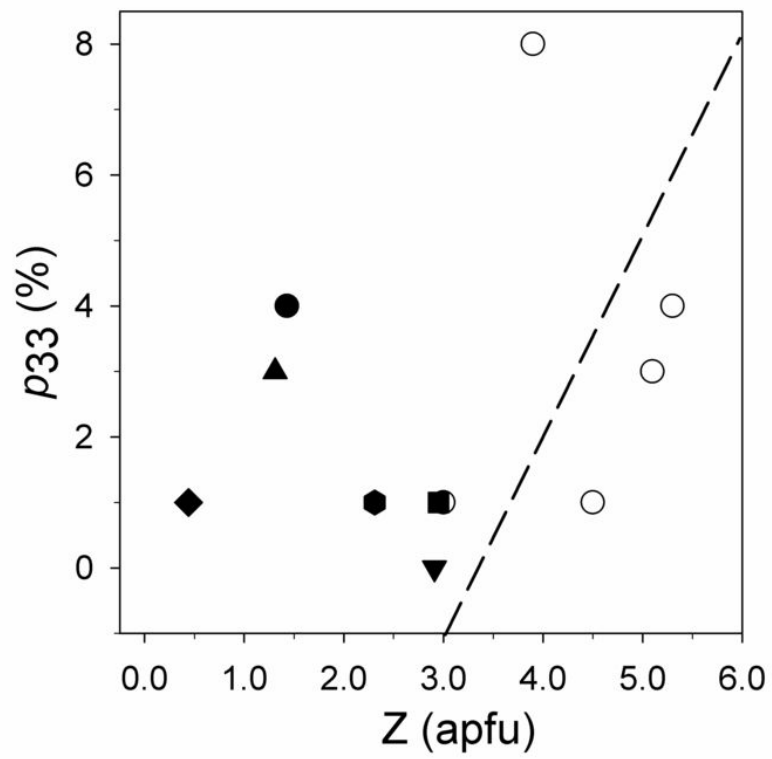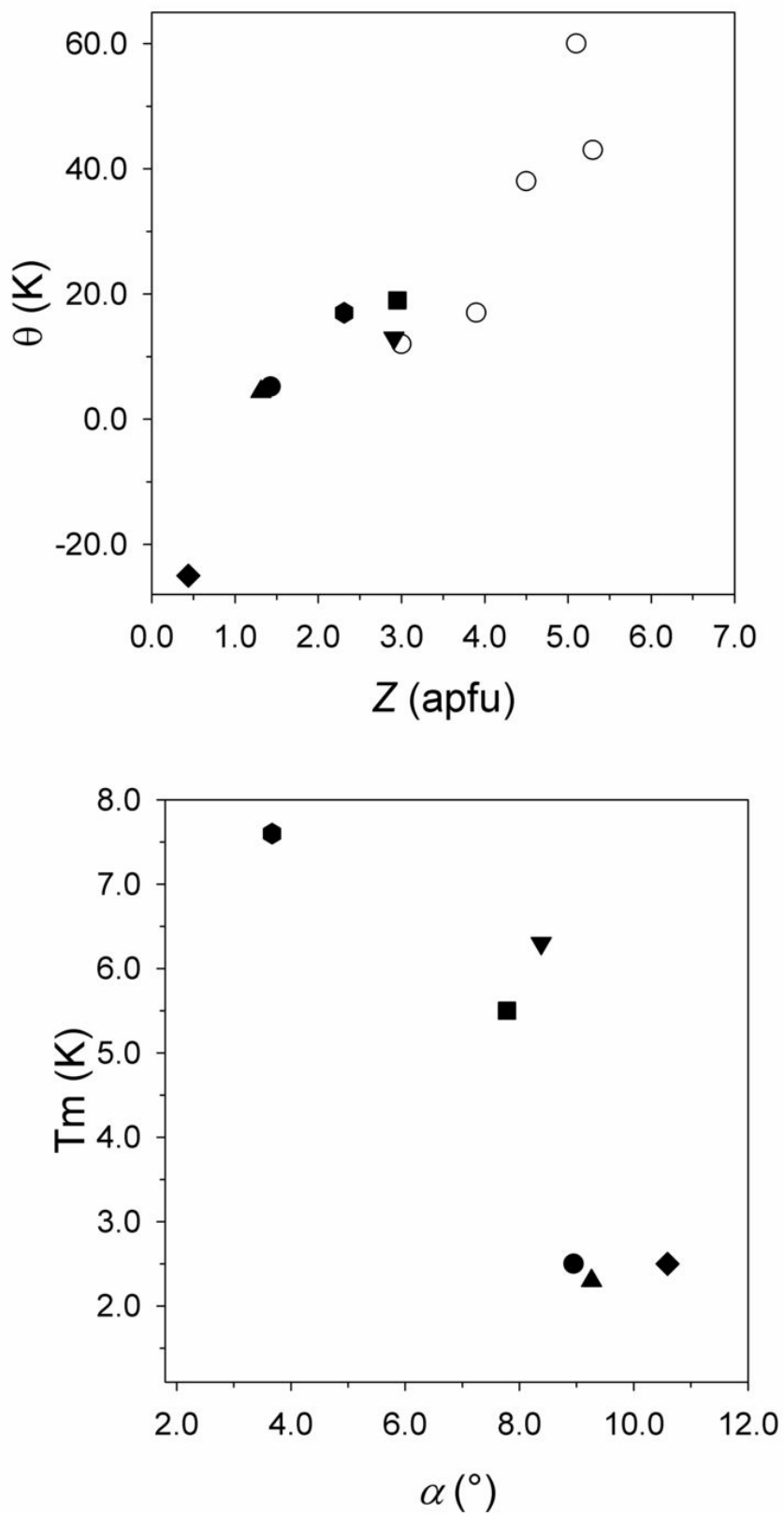
Figure 8

Figure 9

Figure 10

##

Sample	Tapira	Albano	Oquossoc	Bryant Pond	Catalão	Eurajoki
	Chemical composition (oxide wt%)					
SiO_2	38.30	36.40	36.96	34.22	41.52	42.79
TiO_2	2.32	2.10	2.11	2.64	0.23	0.12
Al_2O_3	13.42	16.40	16.81	20.00	0.00	18.71
Fe_2O_3	6.30	5.07	3.05	0.00	17.20	2.28
Cr_2O_3		0.01				
FeO	6.60	6.18	19.80	22.75	2.48	16.73
MnO	0.18	0.20	1.01	0.64	0.03	0.15
MgO	18.15	18.50	6.55	6.03	24.03	0.20
BaO		0.25	0.06			
Li_2O						3.53
Na_2O	0.20	0.30	0.02	0.09	0.03	0.18
K_2O	10.50	10.25	10.12	9.98	10.40	10.40
Rb_2O						0.12
F	0.55	2.42	0.03		1.10	5.96
Cl				0.22		
H_2O	3.70	2.95	3.50	3.50	3.45	1.25
F,Cl=O	-0.23	-1.02	-0.01	-0.05	-0.46	-2.51
Sum	99.99	100.01	100.01	100.02	100.01	99.91
	Unit-cell content (a.p.f.u.)					
$^{[iv]}Si$	2.807	2.660	2.850	2.656	3.102	3.141
$^{[iv]}Al$	1.159	1.340	1.150	1.344		0.859
$^{[iv]}Fe^{3+}$	0.034				0.898	
$^{[iv]}\Sigma$	4.000	4.000	4.000	4.000	4.000	4.000
$^{[vi]}Al$		0.073	0.377	0.485		0.760
$^{[vi]}Mg$	1.982	2.015	0.753	0.697	2.676	0.022
$^{[vi]}Fe^{3+}$	0.313	0.279	0.177		0.069	0.126
$^{[vi]}Fe^{2+}$	0.404	0.378	1.277	1.476	0.155	1.027
$^{[vi]}Cr$		0.001				
$^{[vi]}Mn$	0.011	0.012	0.066	0.042	0.002	0.009
$^{[vi]}Ti$	0.128	0.115	0.122	0.154	0.013	0.007
$^{[vi]}Li$						1.042
$^{[vi]}\Sigma$	2.838	2.873	2.772	2.855	2.915	2.993
$^{[xii]}Na$	0.028	0.043	0.003	0.013	0.004	0.026
$^{[xii]}K$	0.981	0.956	0.995	0.988	0.991	0.974
$^{[xii]}Rb$						0.006
$^{[xii]}Ba$		0.007	0.002			
$^{[xii]}\Sigma$	1.009	1.005	1.000	1.001	0.995	1.005
F	0.127	0.559	0.007		0.260	1.384
Cl				0.029		
OH	1.809	1.438	1.800	1.812	1.719	0.612
O	10.064	10.003	10.193	10.159	10.021	10.004
Σ	12.000	12.000	12.000	12.000	12.000	12.000
	Number of iron atoms (N) per cm^3 of mineral					
N x 10^{21} (moles cm^{-1})	1.50	1.32	2.92	2.96	2.22	2.39
	Curie constant (C) expressed in cgs system.					
C x10^{-3} (emuK/gOe)	6.139	5.497	14.790	14.791	7.458	11.390
	Octahedral sites mean electron count (m.e.c.)					
$M1_{Xref}$	15.4	14.8	19.3	19.8	12.1	14.5
$M2_{Xref}$	15.1	15.1	18.3	18.7	12.6	15.9
$M3_{Xref}$	15.1	15.1	18.3	18.7	12.6	13.0
$M1+M2+M3_{(Xref)}$	45.6	45.0	55.9	57.2	37.3	43.4
$M1+M2+M3_{(Epma)}$	45.5	45.1	56.0	57.5	37.6	43.6
	Interlayer site mean electron count (m.e.c.)					
$A_{(Xref)}$	19.0	19.0	18.9	19.0	18.9	19.0
$A_{(Epma)}$	19.0	19.0	19.0	18.9	18.9	19.0

Table 2. Information related to X-ray data collection, structure refinement and unit cell parameters.

Sample	N_{total}	N_{unique}	R_{int} (%)	$\theta_{(min)}$	$\theta_{(max)}$	Miller index limits	a (Å)	b (Å)	c (Å)	β(°)	V(Å^3)	R(%)
Tapira	2033	830	2.53	2.01	32.14	$-7 \leq h \leq 6, -13 \leq k \leq 13, -15 \leq l \leq 15$	5.3366(4)	9.2421(6)	10.2754(6)	100.012(4)	499.08(6)	3.68
Albano	1999	573	1.78	4.04	27.08	$-6 \leq h \leq 6, -9 \leq k \leq 11, -10 \leq l \leq 13$	5.3303(3)	9.2281(4)	10.2342(5)	99.989(2)	495.77(4)	2.00
Oquossoc	2826	929	3.35	4.04	34.28	$-7 \leq h \leq 7, -13 \leq k \leq 12, -15 \leq l \leq 16$	5.3438(5)	9.2550(7)	10.2390(9)	100.222(4)	498.35(7)	3.78
Bryant Pon	3304	1133	2.06	4.05	35.30	$-8 \leq h \leq 8, -10 \leq k \leq 14, -16 \leq l \leq 16$	5.3473(2)	9.2609(3)	10.2382(3)	100.293(2)	498.84(3)	2.70
Catalão	2928	1107	3.43	4.01	37.91	$-9 \leq h \leq 8, -15 \leq k \leq 10, -16 \leq l \leq 17$	5.380(1)	9.241(2)	10.315(3)	100.08(2)	505.0(2)	3.75
Eurajoki	2094	1069	2.88	4.10	30.80	$-6 \leq h \leq 7, -13 \leq k \leq 10, -14 \leq l \leq 12$	5.3060(5)	9.1636(9)	10.116(1)	100.786(4)	483.17(8)	3.61

Notes: $R_{int} = \sum \left| F_0^2 - F_0^2(mean) \right| / \sum F_0^2 \times 100$; $R = \sum \left\| F_0 \right| - \left| F_c \right\| / \sum \left| F_0 \right| \times 100$.

Table 3a. Relevant cation-anion bond lengths of refined mica crystals, space group C2/m, and selected geometrical parameters obtained from structure refinements.

Sample	Tapira	Albano	Oquossoc	Bryan Pond	Catalão
Tetrahedron					
T-O1	1.661(2)	1.660(1)	1.660(2)	1.660(1)	1.679(2)
T-O1'	1.663(2)	1.663(1)	1.660(2)	1.660(1)	1.674(2)
T-O2	1.663(1)	1.662(1)	1.659(1)	1.660(1)	1.669(1)
T-O3	1.664(2)	1.666(1)	1.679(2)	1.668(1)	1.672(2)
⟨T-O⟩	1.663	1.663	1.665	1.662	1.674
Tetrahedral parameers					
α (°)	8.95	9.26	8.38	7.78	10.59
basal area (A^2)	18.34	18.28	18.41	18.45	18.43
Δz (Å)	0.003	0.004	0.018	0.024	0.006
Volume (A^3)	2.36	2.36	2.37	2.35	2.40
τ (°)	110.26	110.26	110.03	110.2	109.94
⟨O-O⟩$_{basal}$	2.701	2.700	2.701	2.698	2.725
Octahedron (M1)					
M1-O3 (×4)	2.096(1)	2.090(1)	2.103(2)	2.1168(9)	2.102(1)
M1-O4 (×2)	2.060(2)	2.050(1)	2.070(1)	2.086(1)	2.061(2)
⟨M1-O⟩	2.084	2.077	2.092	2.107	2.088
Octahedron (M2)					
M2-O3' (×2)	2.092(2)	2.088(1)	2.078(2)	2.076(1)	2.105(1)
M2-O3 (×2)	2.087(2)	2.085(1)	2.072(2)	2.072(1)	2.090(1)
M2-O4 (×2)	2.063(2)	2.040(1)	2.046(2)	2.044(1)	2.066(1)
⟨M2-O⟩	2.081	2.071	2.065	2.064	2.087
Octahedral parameters					
M1-O4-M2 (°)	96.75(5)	97.41(5)	97.08(6)	96.75(7)	97.42(5)
M1-O4-M2' (°)	96.75(6)	97.41(4)	97.08(6)	96.75(5)	97.42(6)
M2-O4-M2 (°)	96.76(7)	97.18(5)	97.79(5)	98.05(6)	96.63(5)
M1-O3-M2 (°)	109.85(6)	109.62(4)	109.67(5)	109.28(5)	109.96(7)
M1-O3-M2' (°)	120.39(6)	120.91(5)	121.27(6)	121.42(6)	120.76(6)
ψ (M1)°	58.76	59.08	59.47	59.53	58.85
ψ (M2)°	58.70	58.98	59.04	58.84	58.83
⟨O3-O3⟩	3.081	3.077	3.085	3.087	3.093

Interlayer cation

A-O1 (×4)	2.975(2)	2.956(1)	2.983(1)	2.997(1)	2.949(2)
A-O2 (× 2)	2.968(3)	2.958(2)	2.982(2)	2.997(2)	2.957(2)
A-O1' (×4)	3.378(2)	3.377(1)	3.358(1)	3.343(1)	3.431(2)
A-O2' (× 2)	3.383(2)	3.380(2)	3.379(2)	3.370(2)	3.446(2)
$\langle A\text{-}O \rangle_{inner}$	2.973	2.957	2.983	2.997	2.952
$\langle A\text{-}O \rangle_{outer}$	3.380	3.378	3.365	3.352	3.436

Interlayer parameters

$ECoN$	9.38	9.27	9.58	9.70	8.87
A - O4 (Å)	4.018(3)	4.022(2)	4.015(2)	4.009(2)	4.045(2)

Sheet thickness

Tetrahedral (Å)	2.260	2.266	2.267	2.260	2.266
Octahedral (Å)	2.162	2.134	2.125	2.136	2.160
Interlayer separation (Å)	3.436	3.413	3.418	3.417	3.463

Table 3b. Relevant cation-anion bond lengths of sample EP, space group $C2$, and selected geometrical parameters obtained from structure refinements.

Tetrahedra				Interlayer cation	
T1-O1	1.653(8)	T2-O1	1.637(8)	A-O1 (×2)	3.054(3)
T1-O2	1.640(6)	T2-O2	1.659(6)	A-O1' (×2)	3.244(3)
T1-O22	1.627(6)	T2-O22	1.651(5)	A-O2 (×2)	3.024(6)
T1-O3	1.642(6)	T2-O33	1.645(6)	A-O2' (×2)	3.263(7)
⟨T1-O⟩	1.641	⟨T2-O⟩	1.648	A-O22 (×2)	3.063(6)
				A-O22' (×2)	3.131(7)
Tetrahedral parameters				⟨A-O⟩$_{inner}$	3.047
α (°)	3.67	τ (°) (T1)	111.14	⟨A-O⟩$_{outer}$	3.213
basal area (Å^2)	18.21	τ (°) (T2)	111.14		
V(T1) (Å^3)	2.26	Δz (Å)	0.087	Iterlayer parameters	
V(T2) (Å^3)	2.29	Sheet tickness (Å)	2.252	$ECoN$	11.66
				A - O4 (Å)	3.967(3)
				Interlayer separation	3.332

Octahedra					
Octahedron M1		Octahedron M2		Octahedron M3	
M1-O3 (×2)	2.129(8)	M2-O3 (×2)	1.938(7)	M3-O3 (×2)	2.124(5)
M1-O33 (×2)	2.146(7)	M2-O33 (×2)	1.923(5)	M3-O33 (×2)	2.116(7)
M1-O4 (×2)	2.134(4)	M2-O4 (×2)	1.872(5)	M3-O4 (×2)	2.157(5)
⟨M1-O⟩	2.136	⟨M2-O⟩	1.911	⟨M3-O⟩	2.132
Octahedral parameters					
M1-O4-M3	91.50(6)	M1-O3-M3	92.57(5)	ψ (M1)°	60.53
M1-O4-M2	99.93(4)	M1-O33-M2	97.85(6)	ψ (M2)°	56.63
M2-O4-M3	100.44(7)	Sheet tickness (Å)	2.102	ψ (M3)°	60.47

Table 5. Octahedral site population obtained by combining electron microprobe and spectroscopic data and taking into account the results of structure refinement.

Sample	Tapira	Albano	Oquossoc	Bryant Pond	Catalão	Eurajoki
M1 site						
$^{[vi]}Mg$	0.455	0.580	0.046	0.169	0.828	0.004
$^{[vi]}Fe^{3+}$	0.314	0.278	0.176		0.069	
$^{[vi]}Fe^{2+}$	0.058	0.012	0.484	0.643	0.016	0.500
$^{[vi]}Mn$	0.011	0.012	0.066	0.042	0.002	
$^{[vi]}Li$						0.489
vacancies	0.162	0.118	0.228	0.146	0.085	0.007
$^{[vi]}\Sigma$	1.000	1.000	1.000	1.000	1.000	1.000
M2 site						
$^{[vi]}Al$		0.037	0.189	0.243		0.760
$^{[vi]}Mg$	0.763	0.718	0.354	0.264	0.924	0.013
$^{[vi]}Fe^{3+}$						0.126
$^{[vi]}Fe^{2+}$	0.173	0.183	0.396	0.416	0.069	0.085
$^{[vi]}Cr$		0.005				
$^{[vi]}Mn$						0.009
$^{[vi]}Ti$	0.064	0.057	0.061	0.077	0.007	0.007
$^{[vi]}\Sigma$	1.000	1.000	1.000	1.000	1.000	1.000
M3 site						
$^{[vi]}Al$		0.037	0.189	0.243		
$^{[vi]}Mg$	0.763	0.718	0.354	0.264	0.924	0.005
$^{[vi]}Fe^{3+}$						
$^{[vi]}Fe^{2+}$	0.173	0.183	0.396	0.416	0.069	0.442
$^{[vi]}Cr$		0.005				
$^{[vi]}Mn$						
$^{[vi]}Ti$	0.064	0.057	0.061	0.077	0.007	
$^{[vi]}Li$						0.553
$^{[vi]}\Sigma$	1.000	1.000	1.000	1.000	1.000	1.000

Table 5.　Crystal chemical and magnetic parameters for studied samples andfor some phyllosilicates reported in the literature.

Sample	S	layer type	Z	θ	Tm	θ/Tm		Reference
Chamosite	7.1	1:1	3	12	8	1.5	SG	Ballet et al. (1985)
Minnesotaite	9.6	2:1	4.5	38	19	2	AF	Ballet et al. (1985)
Biotite	10	2:1	5.3	43	7	6.1	SG	Ballet and Coey (1982)
Thuringite	7.1	2:1:1	3.9	17	5	3.4	SG	Ballet et al. (1985)
Annite	10	2:1	5.1	60	58	1	AF	Rancourt et al. (1994)
Tapira	10.24	2:1	1.43	5.2	2.5	2.1	SG	
Albano	10.24	2:1	1.31	4.4	2.3	1.9	SG	
Oquossoc	10.23	2:1	2.91	13	6.3	2.1	SG	
Bryant Pond	10.28	2:1	2.95	19	5.5	3.5	SG	
Catalão	10.32	2:1	0.44	-25	2.5	-10.0	PM	
Eurajoki	10.12	2:1	2.31	17	7.6	2.2	SG	

S = distance between two magnetic sheets. Z = octahedral Fe atoms per unit cell; θ = Curie-Weiss constant; Tm = temperature of magnetic suscptivity maximum; AF = planar antiferromagnetic behavior; SG = spin glass behavior; PM = paramagnetic behavior.